THE NGC 404 NUCLEUS: STAR CLUSTER AND POSSIBLE INTERMEDIATE-MASS BLACK HOLE

Anil C. Seth[1,9], Michele Cappellari[2], Nadine Neumayer[3], Nelson Caldwell[1], Nate Bastian[4], Knut Olsen[5],
Robert D. Blum[5], Victor P. Debattista[6], Richard McDermid[7], Thomas Puzia[8], and Andrew Stephens[7]

[1] Harvard-Smithsonian Center for Astrophysics, 60 Garden Street Cambridge, MA 02138, USA; aseth@cfa.harvard.edu
[2] Sub-department of Astrophysics, University of Oxford, Denys Wilkinson Building, Keble Road, Oxford, OX1 3RH, UK
[3] European Southern Observatory, Karl-Schwarzschild-Str. 2, 85748 Garching, Germany
[4] Institute of Astronomy, University of Cambridge, Madingley Road, Cambridge CB3 0HA, UK
[5] National Optical Astronomy Observatory, 950 North Cherry Ave., Tucson, AZ 85719, USA
[6] Jeremiah Horrocks Institute, University of Central Lancashire, Preston, Lancashire, PR1 2HE, UK
[7] Gemini Observatory, 670 N. A'ohoku Place Hilo, HI 96720, USA
[8] Herzberg Institute of Astrophysics, 5071 West Saanich Road, Victoria, BC V9E 2E7, Canada

ABSTRACT

We examine the nuclear morphology, kinematics, and stellar populations in nearby S0 galaxy NGC 404 using a combination of adaptive optics assisted near-IR integral-field spectroscopy, optical spectroscopy, and *Hubble Space Telescope* imaging. These observations enable study of the NGC 404 nucleus at a level of detail possible only in the nearest galaxies. The surface brightness profile suggests the presence of three components: a bulge, a nuclear star cluster (NSC), and a central light excess within the cluster at radii < 3 pc. These components have distinct kinematics with modest rotation seen in the NSC and counter-rotation seen in the central excess. Molecular hydrogen emission traces a disk with rotation nearly orthogonal to that of the stars. The stellar populations of the three components are also distinct, with half of the mass of the NSC having ages of ∼1 Gyr (perhaps resulting from a galaxy merger), while the bulge is dominated by much older stars. Dynamical modeling of the stellar kinematics gives a total NSC mass of $1.1 \times 10^7 \, M_\odot$. Dynamical detection of a possible intermediate-mass black hole (BH) is hindered by uncertainties in the central stellar mass profile. Assuming a constant mass-to-light ratio, the stellar dynamical modeling suggests a BH mass of $< 1 \times 10^5 \, M_\odot$, while the molecular hydrogen gas kinematics are best fitted by a BH with a mass of $4.5^{+3.5}_{-2.0} \times 10^5 \, M_\odot$. Unresolved and possibly variable dust emission in the near-infrared and active galactic nucleus-like molecular hydrogen emission-line ratios do suggest the presence of an accreting BH in this nearby LINER galaxy.

Key words: galaxies: elliptical and lenticular, cD – galaxies: formation – galaxies: individual (NGC 404) – galaxies: kinematics and dynamics – galaxies: nuclei – galaxies: structure

Online-only material: color figures

1. INTRODUCTION

The centers of galaxies contain both massive black holes (MBHs) and nuclear star clusters (NSCs). The presence of MBHs has been dynamically measured in about 50 galaxies and it appears that most massive galaxies probably have an MBH (e.g., Richstone et al. 1998; Graham 2008). Nuclear star clusters are compact ($r_{\rm eff} \sim 5$ pc), massive (∼$10^7 \, M_\odot$) star clusters found at the center of a majority of spirals and lower mass ellipticals (Böker et al. 2002; Carollo et al. 2002; Côté et al. 2006). Unlike normal star clusters, they have multiple stellar populations with a wide range of ages (Long et al. 2002; Walcher et al. 2006; Rossa et al. 2006; Seth et al. 2006; Siegel et al. 2007). Nuclear star clusters coexist with MBHs in some galaxies (Filippenko & Ho 2003; Seth et al. 2008a; Shields et al. 2008; Graham & Spitler 2009). However, the nearby galaxies M33 and NGC 205 have NSCs but no apparent central black hole (BH; Gebhardt et al. 2001; Valluri et al. 2005), while some high-mass core elliptical galaxies have MBHs but lack NSCs (Côté et al. 2006).

Occupation fractions and masses for MBHs in lower mass galaxies retain the imprint of the seed BHs from which they form, information which has been lost due to subsequent accretion in higher mass galaxies (e.g., Volonteri et al. 2008). However, the presence and mass of MBHs in lower mass galaxies are very poorly constrained. Most galaxies are too far away to measure the dynamical effect of a BH with mass $\lesssim 10^6 \, M_\odot$ (often referred to as intermediate-mass black holes; IMBHs) with current instrumentation. Thus the presence of IMBHs in galaxy centers has only been inferred when active galactic nucleus (AGN) activity is observed (e.g., Filippenko & Sargent 1989; Greene & Ho 2004; Satyapal et al. 2007). These AGNs provide only a lower limit on the number of MBHs in lower mass galaxies, and the BH mass estimates from the AGN are quite uncertain.

Dynamical measurements of MBHs in nearby massive galaxies have revealed that the mass of a galaxy's central MBH is correlated with its bulge mass (Kormendy & Richstone 1995; Magorrian et al. 1998; Häring & Rix 2004). The scaling of BH mass with the large-scale properties of galaxies extends to many measurable quantities including the bulge velocity dispersion (Ferrarese et al. 2000; Gebhardt et al. 2000; Graham 2008; Gültekin et al. 2009). More recently, Ferrarese et al. (2006), Wehner & Harris (2006), and Rossa et al. (2006) have presented evidence that NSCs scale with bulge mass and dispersion in elliptical and early-type spiral galaxies in almost exactly the same way as MBHs.

The similarity between the NSC and MBH scaling relationships led Ferrarese et al. (2006) and Wehner & Harris (2006) to suggest that MBHs and NSCs are two different types of central massive objects (CMOs), both of which contain a small fraction (∼0.2%) of the total galaxy mass. This correlation of the CMO

---

[9] OIR fellow.

Table 1
NGC 404 Properties

Distance[a]	3.06 Mpc
$m-M$	27.43
pc arcsec^{-1}	14.8
Galaxy $M_{V,0}$, $M_{I,0}$[b]	-17.35, -18.36
Bulge/total luminosity[c]	0.76
Bulge $M_{V,0}$, $M_{I,0}$[d]	-17.05, -18.06
Bulge mass[e]	$9.2 \times 10^8\ M_\odot$
H I gas mass[f]	$1.5 \times 10^8\ M_\odot$
Molecular gas mass[g]	$6 \times 10^6\ M_\odot$
Central velocity[h]	-58.9 km s^{-1}

Notes.
[a] TRGB measurement from Karachentsev et al. (2004).
[b] At $r < 200''$, from Tikhonov et al. (2003) corrected for foreground reddening.
[c] For $r < 200''$, from Baggett et al. (1998).
[d] Combining above values, we derive a slightly brighter bulge $M_{I,0} = -18.20$ in Section 3.
[e] Using $M/L_I = 1.28$ from Section 5.4.
[f] del Río et al. (2004).
[g] Wiklind & Henkel (1990), corrected to $D = 3.06$ Mpc.
[h] Heliocentric velocity; see Section 4.1.

mass with the large-scale properties of galaxies suggests a link between the formation of the two. However, the nature of this connection is unknown, as is the relation between NSCs and MBHs. Studies of NSCs can help address these issues. Their morphology, kinematics, and stellar populations contain important clues about their formation and the accretion of material into the center of galaxies (e.g., Hopkins & Quataert 2010).

The scaling relationships of large-scale galaxy properties with the mass of the CMO might indicate that galaxy centers should be simple systems. The Milky Way center clearly shows this not to be the case. It is an incredibly complicated environment with a BH ($M_{BH} = 4 \times 10^6\ M_\odot$; Ghez et al. 2008) and an NSC ($M_{NSC} \sim 3 \times 10^7\ M_\odot$; Genzel et al. 1996; Schödel et al. 2007; Trippe et al. 2008) that contains stars of many ages and in different substructures including disks of young stars in the immediate vicinity of the BH (e.g., Lu et al. 2009; Bartko et al. 2009). Only through understanding these complex structures in the Milky Way and finding other examples in nearby galaxies can we hope to fully understand MBH and NSC formation, and the links between these objects and their host galaxies.

In our current survey, we are looking at a sample of the nearest galaxies ($D < 5$ Mpc) that host NSCs. We are resolving their properties using a wide range of observational data to understand how NSCs form and their relation to MBHs. In our first paper, on nearby edge-on spiral NGC 4244 (Seth et al. 2008b), we showed evidence that the NSC kinematics are dominated by rotation, suggesting that it was formed by episodic accretion of material from the galaxy disk.

This paper focuses on the NSC and possible MBH in NGC 404, the nearest S0 galaxy. Table 1 summarizes its properties. The stellar populations of the galaxy are predominantly old and can be traced out to $600''$ (9 kpc; Tikhonov et al. 2003; Williams et al. 2010). However, H I observations show a prominent nearly face-on H I disk at radii between $100''-400''$, with detectable H I out to $800''$ (del Río et al. 2004). CO observations and optical color maps show the presence of molecular gas and dust within the central $\sim 20''$ (300 pc) of the galaxy (Wiklind & Henkel 1990; Tikhonov et al. 2003), lying primarily to the NE of the nucleus. An NSC in the central arcsecond of NGC 404

was noted by Ravindranath et al. (2001) from an analysis of NICMOS data.

The presence of an AGN in NGC 404 is a controversial topic. The optical spectrum of the nucleus has line ratios with a LINER classification (Ho et al. 1997). Assuming a distance of ~ 3 Mpc, NGC 404 is the nearest LINER galaxy; other nearby examples include M81 and NGC 4736 (M94). Recent studies have shown that most LINERS do in fact appear to be AGNs, with a majority of them having detected X-ray cores (Dudik et al. 2005; González-Martín et al. 2006; Zhang et al. 2009), radio cores (Nagar et al. 2005), and many of them possessing mid-IR coronal lines (Satyapal et al. 2004) and UV variable cores (Maoz et al. 2005). However, NGC 404 is quite unusual in its properties. No radio core is observed down to a limiting flux of 1.3 mJy at 15 GHz with the VLA in A array (Nagar et al. 2005); however, del Río et al. (2004) do detect an unresolved 3 mJy continuum source at 1.4 GHz using the C array. A compact X-ray source is detected (Lira et al. 2000; Eracleous et al. 2002), but its low luminosity and soft thermal spectrum indicate that it could be the result of a starburst. Signatures of O stars are seen in the UV spectrum of the nucleus; however, dilution of these lines suggests that $\sim 60\%$ of the UV flux could result from a nonthermal source (Maoz et al. 1998). This suggestion is supported by more recent UV observations which show that the UV emission is variable, declining by a factor of ~ 3 between 1993 and 2002 (Maoz et al. 2005). *Hubble Space Telescope* (*HST*) observations of Hα show that the emission occurs primarily in a compact source $0''.16$ north of the nucleus and in wispy structures suggestive of supernova remnants (Pogge et al. 2000). The [O III] emission has a double-lobed structure along the galaxy major axis (Plana et al. 1998) and has a higher velocity dispersion than Hα near the galaxy center (Bouchard et al. 2010). The mid-IR spectrum of NGC 404 shows evidence for high excitation consistent with other AGNs (Satyapal et al. 2004). In particular, the ratio of the [O IV] flux relative to other emission lines ([Ne II], [Si II]) is higher than any other LINERs in the Satyapal et al. (2004) sample and is similar to other known AGNs. However, [Ne V] lines, which are a more reliable indicator of AGN activity (Abel & Satyapal 2008), are not detected. In summary, the case for an accreting MBH in NGC 404 remains ambiguous, with the variable UV emission providing the strongest evidence in favor of its existence.

In this paper, we take a detailed look at the central arcseconds of NGC 404 and find evidence that it contains both a massive NSC and a BH. In Section 2, we describe the data used in this paper including adaptive optics Gemini/NIFS observations. We then use these data to determine the morphology in Section 3, the stellar and gas kinematics in Section 4, and the stellar populations in Section 5. In Section 6, we present dynamical modeling from which we derive an NSC mass of $1.1 \times 10^7\ M_\odot$ and find mixed results on detecting a possible MBH with mass $<10^6\ M_\odot$. In Section 7 we discuss these results, concluding in Section 8.

2. OBSERVATIONS AND REDUCTION

This paper presents a combination of a wide variety of data including: (1) high spatial resolution near-infrared Integral Field Unit (IFU) spectroscopy with Gemini's Near-Infrared Integral Field Spectrometer (NIFS), (2) optical long-slit spectra from the MMT, and (3) *HST* imaging data from the UV through the NIR. Using these data we have determined the morphology, gas and stellar kinematics, and stellar populations of the central regions
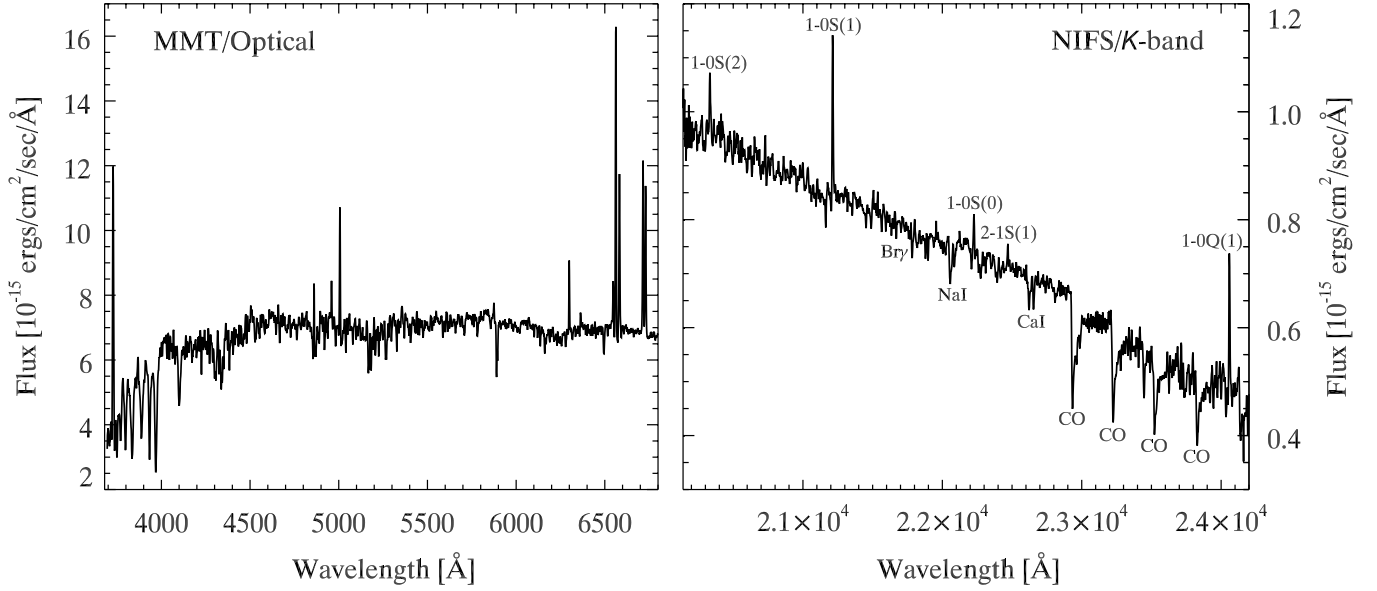
Figure 1. Left: optical spectrum of the NGC 404 NSC ($1'' \times 2''.3$ aperture) taken with the BCS on the MMT. Right: K-band spectrum of the NGC 404 NSC using a $1''$ radius aperture from our Gemini/NIFS data. Emission lines of H_2 are labeled above the spectrum (see Section 3.2), while strong absorption features are labeled below the spectrum (including Brγ which is seen weakly in absorption and emission; see Figure 6).

of NGC 404. In this section, we describe these data and their reduction.

2.1. Gemini NIFS Data

Observations of NGC 404 with Gemini's NIFS are part of an ongoing survey of nearby NSCs. The data were taken using the Altair laser guide star (LGS) system on the Gemini North telescope on the nights of 2008 September 21 and 22. The nucleus itself was used as a tip-tilt star. A total of 12 760 s exposures were obtained; half were dithered on-source exposures while the others were sky exposures offset by $131''$ to the northwest taken after each on-source exposure. A telluric calibrator, HIP 1123, an A1 star, was observed both nights at an air mass similar to the observations.

The data were reduced using the Gemini version 1.9 IRAF package, utilizing pipelines based on the NIFSEXAMPLES scripts. Ronchi mask and arc lamp images were used to determine the spatial and spectral geometry of the images. The sky images were subtracted from their neighboring on-source images, and then these images were flat-fielded, had bad pixels removed, and were split apart into long-slit slices. The spectra were then divided by the telluric calibrator (using NFTEL-LURIC) after correcting for the Brγ absorption in the calibrator. We made minor alterations to the Gemini pipeline to enable propagation of the variance spectrum. This also required creation of our own IDL version of the NIFCUBE to make the final data cubes. In this process, the initial pixel size of the data, $0''.103$ in the vertical direction and $0''.045$ in the horizontal direction, was rebinned to $0''.05 \times 0''.05$ pixels in the final data cube for each on-source exposure. Data cubes for the six dithered exposures were then shifted spatially and combined with cosmic-ray rejection using our own IDL program. Data from the second night were spectrally shifted to the wavelength solution of the first night before combining. The heliocentric correction was nearly identical on both nights ($+13.25$ km s^{-1}). The NIFS spectrum within a $1''$ aperture is shown in Figure 1 and shows strong absorption and emission lines.

We also processed the sky frames in a manner identical to the on-source exposures. We used the resulting data to calibrate the spectral resolution of our observations. Using 13 isolated, strong, doublet sky lines, we measured the spectral resolution of each pixel in our final data cube. We found significant variations in the spectral resolution across the detector, with a median resolution of 4.36 Å FWHM ($\lambda/\Delta\lambda = 5275$), and values ranging from 3.9 to 5.1 Å FWHM.

A K-band image was made by collapsing all channels after multiplying by (1) a 9500 K blackbody to correct for the shape of the telluric spectrum and (2) the Two Micron All Sky Survey (2MASS) response curve. Flux calibration was obtained from 2MASS by deriving a zero point from images of both sources and calibrators in our sample. We flux-calibrated our spectra using synthetic 2MASS photometry of our telluric calibrator HIP 1123, assuming its spectral shape resembles that of a 9500 K blackbody. From this flux calibration we obtained a flux-calibrated spectrum of our NGC 404 NIFS data cube with units of erg s^{-1} cm^{-2} Å^{-1}. The flux calibration of the image and spectrum is good to $\sim$10%.

2.1.1. PSF Determination

Understanding the point-spread function (PSF) is important for interpreting the kinematic observations presented in Section 4 and is even more critical for the dynamical modeling in Section 6. We used two methods for measuring the PSF of the calibrator: (1) we created images from the telluric calibrator for both nights to estimate the PSF, and (2) we compared the final NIFS K-band images of the NGC404 nucleus to *HST F814W* data.

We initially tried modeling the PSF as a double Gaussian (as in Krajnović et al. 2009). However, double Gaussians were a very poor fit to the wings of the PSF in the telluric calibrator images. Using an inner Gaussian + outer Moffat profile ($\Sigma(r) = \Sigma_0/[1 + (r/r_d)^2]^{4.765}$) adequately described the telluric calibrator PSF. The best fit on both nights was a PSF with an inner Gaussian FWHM of $0''.12$, and an outer Moffat profile r_d of $0''.95$, each containing about half the light. The two
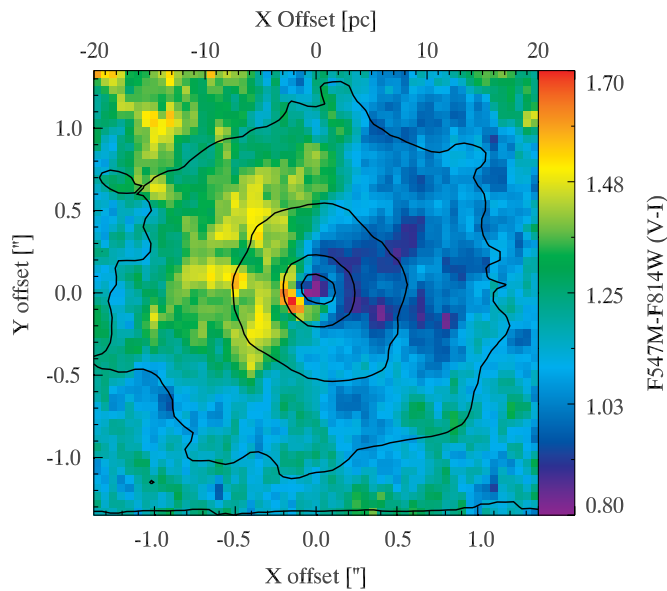
Figure 2. *HST* WFPC2 *F547M − F814W* (approximately *V−I*) color map of the nuclear region. Contours show the NIFS continuum emission at μ_K of 11.2, 12.2, 13.2, 14.2, and 15.2 mag arcsec^{-2}. The image is centered on the dust-corrected peak of the continuum light with north up and east to the left. Redder regions result from dust extinction. The western half of the nucleus appears to have little internal extinction (see Section 5.2).

(A color version of this figure is available in the online journal.)

nights' PSFs were very similar (< 10% differences) in both shape and fraction of light in each component. Unfortunately, our telluric images were not well dithered and thus the central PSF is not well sampled.

We further refined the PSF by fitting a convolved version of the *F814W*-band *HST* image to the NIFS *K*-band image. Although *HST*/NIC2 and NIC3 *F160W* data were also available, the larger pixel scale and the limited resolution of *HST* in the NIR (FWHM~0″.14) make the *F814W* data a better image to use as a PSF reference. Due to the dust around the nucleus, we fit only the western, apparently dust free, half of the nucleus (Figure 2). Also, we find in Section 3.1 that the NIFS image contains compact non-stellar emission from hot dust at the center; we therefore correct the *K*-band image for this dust emission before determination of the PSF. Finally, because the profile of the galaxy is much shallower than the PSF, we fix the functional form of the outer profile to that derived for the telluric star, but allow the inner PSF width and fraction of light in each component to vary. The best-fitting PSF has a core with FWHM~ 0″.09 (assuming an *HST* resolution of 0″.065 based on TinyTim models; Krist 1995) containing 51% of the light, with the outer Moffat (with $r_d = 0″.95$) function containing 49% of the light.

This PSF suffers from a number of uncertainties. Most notably, the presence of a bluer population at the center of the cluster implied by Figure 2 may make the *F814W* image more centrally concentrated relative to the dust-corrected *K*-band image. Due to our fitting the NIFS PSF core to a convolution of the *F814W* image, this effect could lead to an overestimate in the core FWHM.

2.1.2. Stellar Kinematics Determination

Derivation of the stellar kinematics was done as described in Seth et al. (2008b) with a couple of additions. In brief, we first spatially binned the data to a target signal-to-noise ratio (S/N) of 25 using the Voronoi tesselation method described in Cappellari & Copin (2003). The S/N of the data was as high as 175 in the center, and data within ~ 0″.7 were left unbinned. Next, we determined the stellar line-of-sight velocity distribution (LOSVD) using the penalized pixel fitting of Cappellari & Emsellem (2004) to derive the velocity, dispersion, $h3$, and $h4$ components in the wavelength region from 22850 Å to 23900 Å. We used high-resolution templates from Wallace & Hinkle (1996) which has supergiant, giant, and main-sequence stars between spectral types G and M; we used eight of these stars with the most complete wavelength coverage. These templates were convolved to the instrumental resolution measured in each pixel from the sky lines before fitting the LOSVD. Nearly identical kinematic results and fit qualities were obtained using the larger GNIRS library (Winge et al. 2009) as templates. We performed LOSVD fits over different ranges of wavelengths and with different subsets of templates and achieved consistent results, suggesting template mismatch is not a significant issue. We used the Wallace & Hinkle (1996) templates rather than the Winge et al. (2009) templates due to their higher spectral resolution and more accurate velocity zero point. Errors on the LOSVD were calculated by taking the standard deviation of values derived from 100 Monte Carlo simulations in which appropriate levels of Gaussian random noise were added to each spectral pixel before remeasuring the LOSVD. Errors on the radial velocities ranged from 0.5 to 6 km s^{-1}, depending primarily on the S/N.

2.2. Optical Spectroscopy

Optical spectroscopy of the NGC 404 cluster was obtained (along with spectra of other nearby NSCs) with the blue channel spectrograph (BCS) on the MMT 6.5 m telescope on the night of 2009 January 19. We used the 500 line grating and a 1″ slit to obtain a resolution of ~3.6 Å FWHM between 3680 Å and 6815 Å with a pixel size of 0″.3 spatially and 1.17 Å spectrally. Two 1200 s exposures were taken, with one being affected by clouds. Due to variations in the slit width, flat-fielding of the data was accomplished by carefully constructing a composite flat field using the pattern from quartz flats taken just after the exposure with pixel-to-pixel information drawn from flats throughout the night. Wavelength calibration was done using arcs taken just after the science exposures. Spectral extraction was accomplished using the standard IRAF DOSLIT routine using optimal extraction over the central 2″.3 of the slit while sky regions were selected to avoid regions of emission near the nucleus. Guide camera seeing was around 0″.8; however, within the instrument it appeared to be significantly larger (~ 1″.7). Three flux calibrators, Gliese 191B2B, HZ44, and VMa2 (Bessell 1999), were observed on the same night with the same observing setup. Flux calibration was achieved by combining information from all three flux calibrators using SENSFUNC. Final residuals between the fitted sensitivity function and the three calibrators were <0.03 mag between 3680 Å and 6200 Å. We note that second-order contamination was present beyond 6200 Å. One of the NGC 404 exposures and 2/3 calibrator exposures were affected by clouds. However, by scaling to the clear exposures, the absolute calibration of the spectra appears to be quite good; comparison of emission-line fluxes to those in Ho et al. (1997) shows agreement to within 5% through a similar size aperture. The S/N per pixel of the final combined spectrum ranged from 100 at 3700 Å to 250 around 5000 Å. The extracted nuclear spectrum is shown in Figure 1.
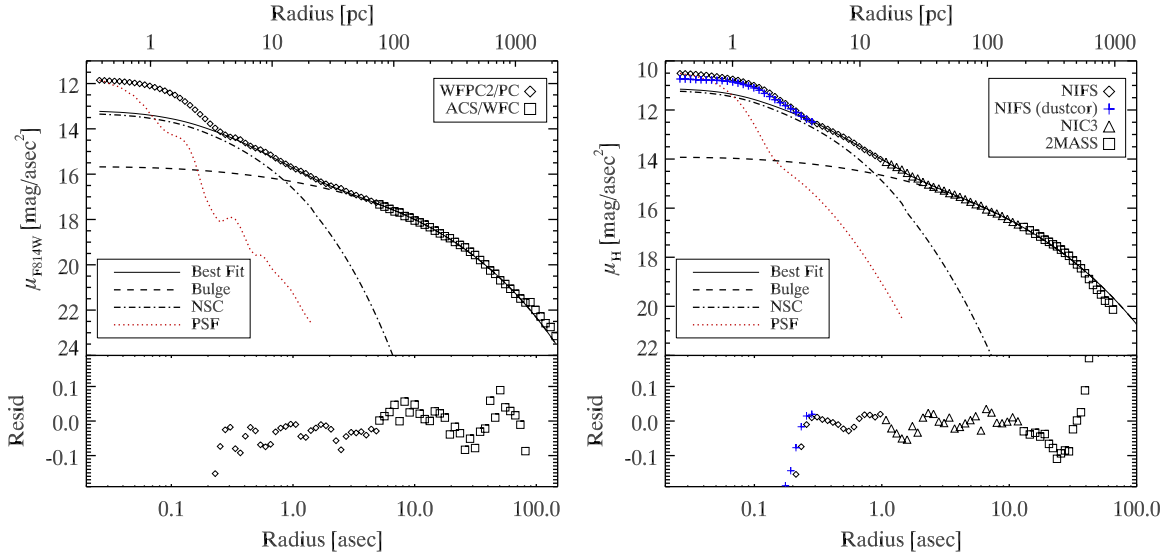
Figure 3. Surface brightness profiles of NGC 404 created from *HST*, Gemini/NIFS, and 2MASS data. In both panels, the observed SB profiles are plotted with symbols: the solid line shows the best-fit two-Sérsic model, the dashed line the outer (bulge) component, and the dot-dashed line the inner (NSC) component. The PSF is shown as a dotted red line in both plots. Residuals disappear off the plot at small radii to the unmodeled extra-light component. Left: the *F814W* profile constructed from both WFPC2/PC (diamonds) and ACS/WFC (squares) data. These data are the most reliable data available at large radii. Right: the NIR profile constructed from three images: NIFS *K* band (diamonds), *HST* NICMOS/NIC3 (triangles), and 2MASS large galaxy atlas data (squares; Jarrett et al. 2003). Blue diamonds show a correction for hot-dust emission discussed in Section 3.1.

(A color version of this figure is available in the online journal.)

2.3. HST Data

A wide variety of *HST* data are available for the nucleus of NGC 404 taken with the Faint Object Spectrograph (FOS), WFPC2, NICMOS, and Advanced Camera for Surveys (ACS) High Resolution Channel (HRC), and Wide Field Channel (WFC). In this paper, we will use WFPC2 data in the *F547M*, *F656N* (PID: 6871), *F555W*, and *F814W* (PID: 5999) filters, ACS WFC data in the *F814W* filter (PID: 9293) and NICMOS NIC2 and NIC3 data in the *F160W* filter (PID: 7330 & 7919). Data were downloaded from the *HST* archive and the Hubble Legacy Archive (HLA). The WFPC2 data all had the nucleus in the PC chip and were unsaturated, while the ACS *F814W* data are saturated at the center but cover the galaxy to larger radii than the WFPC2 data. Astrometric alignment of these data and the NIFS data was tied to the *F814W* WFPC2 data. The centroided position of the nucleus was used to align each image to the *F814W* data. Although dust clearly affects the area around the nucleus, the *F547M* − *F814W* color map (Figure 2) and the alignment of sources in the NIFS Brγ map with the *HST* Hα image (see Section 3.2) suggest that the very center of the galaxy does not suffer from significant internal dust extinction.

3. MORPHOLOGY

To determine the extent and luminosity of the NSC in NGC 404, it is necessary to fit the relatively steep surface brightness (SB) profile of the inner part of the galaxy. Using Sérsic fits to *I*- and *H/K*-band data, we find evidence that an NSC dominates the central 1″ (15 pc) of the galaxy and that an additional emission component appears to be present within the central few parsecs (see Figure 3).

Before describing our results on the central parts of the galaxy, we summarize previous studies of the large-scale light profile of NGC 404. Using ground-based *V*-band data out to nearly 300″, Baggett et al. (1998) decompose the SB profile of NGC 404 into an $r^{1/4}$ bulge and an exponential disk. They find a bulge effective

radius of 64″ and a disk with scale length of 130″. The bulge dominates the light out to ∼150″ and the bulge-to-total ratio is ∼0.7. Tikhonov et al. (2003) found that the number counts of red giant branch stars between 100″–500″ (1.5–7.5 kpc) are also well explained by an exponential disk with a similar ∼106″ scale length.

We used archival *HST* data, our NIFS *K*-band image, and the 2MASS Large Galaxy Atlas (Jarrett et al. 2003) to construct the two SB profiles shown in Figure 3. Surface brightness measurements were obtained on all images using the `ellipse` program in IRAF. The *F814W*-band (*I*) profile combines *HST* WFPC2 data from the PC chip at radii below 5″ with ACS/WFC data at larger radii (the ACS image was saturated at smaller radii). Diffraction spikes from β And (7′ to the SE) and bright foreground stars and background galaxies were masked. Dust is obviously present near the center, and this was masked out as well as possible using an *F555W* − *F814W* color map at radii between 0.″3 and 5″ from the center. Comparing this profile with the NIR light profile suggests that some dust extinction remains within the inner 1″. The NIR profile combines the NIFS *K*-band image (at *r* ≤ 1″), with the *F160W*-band (*H*) NICMOS/NIC3 image (1 < *r* ≤ 5″) and *H*-band data from the 2MASS Large Galaxy Atlas (at *r* > 5″). The NIFS data were scaled to match the *H*-band zero point; no scaling was needed to match the 2MASS and NICMOS data. The final *F814W* and NIR SB profiles are shown in Figure 3.

We first fit the outer part of both profiles to a Sérsic profile (see Graham & Driver 2005 for a complete discussion of Sérsic profiles). During our fitting, the Sérsic profiles were convolved with the PSF. The 2MASS data were only usable to 70″ due to low S/N, and even within this radius the sky subtraction is suspect due to nearby β And. The *F814W* data are more reliable at these larger radii; however, we fit only the measurements within 80″ due to uncertainty in the sky background and possible contribution from a disk at larger radii. At radii beyond 5″, the profiles are well fitted by similar Sérsic profiles with *n* ∼ 2.5

Table 2
Morphological Fits

Component	Sérsic n	$r_{\rm eff}$ ["]	$\mu_{\rm eff,\,F814W}$ (mag arcsec^{-2})	M_I
F814W profile				
Bulge	2.43	41.5	20.18	−18.09
NSC	1.99	0.74	16.02	−13.64
Central excess				−11.81

Component	Sérsic n	$r_{\rm eff}$ ["]	$\mu_{\rm eff,\,H}$ (mag arcsec^{-2})	M_H
NIR profile				
Bulge	2.71	44.7	18.82	−19.62
NSC	2.61	0.68	14.15	−15.34
Central excess				−12.61
Central excess (dust corrected)				−12.14

Notes. Bulge magnitudes given for $r \leqslant 80''$ and NSC magnitudes for $r \leqslant 3''$. Central excess magnitudes are for the total flux above the fit in the central arcsecond. Distance modulus is assumed to be 27.43 giving $1''=14.8$ pc. Note that the magnitudes are not corrected for foreground extinction ($A_I = 0.11$, $A_H = 0.03$; Schlegel et al. 1998).

and effective (half-light) radius of $\sim 43''$ (640 pc). Exact values for all fits are given in Table 2. We identify this outer component as the bulge given the results of Baggett et al. (1998), who show that the bulge component dominates at $r \lesssim 150''$. It was not possible to fit either profile down to smaller radii with a single Sérsic.

Following Graham & Guzmán (2003) and Côté et al. (2006), we identify the excess light over the bulge at small radii to be an NSC. We discuss the nature of this component more in Section 7.1. In both profiles, the NSC component is brighter than the bulge at $r < 1''$. We fit this component with an additional Sérsic component (following Graham & Spitler 2009) and find that it has an effective radius of $\sim 0''.7$ (10 pc). The NSC Sérsic n value is quite sensitive to the functional form of the PSF; therefore, we prefer the *F814W* value of $n = 1.99$ due to the better-known PSF. These parameters are in the ranges typical of NSCs (Côté et al. 2006; Graham & Spitler 2009) in other galaxies. The absolute magnitude of this component (based on the model) is M_I, $M_H = -13.64$, -15.34 within the central $3''$, and M_I, $M_H = -13.17$, -14.93 within $1''$.

In the inner $0''.2$, there is a clear excess luminosity above the double-Sérsic fit in both profiles. Adding up the light in excess of the profile we find an M_I, $M_H = -11.81$, -12.61. Note that these magnitudes are quite sensitive to the PSF and Sérsic n indices of the NSC fit. We will show below that in the NIR, a fraction of this light appears to be emitted by hot 950 K dust. A correction for this dust emission is shown with blue diamonds in Figure 3. However, dust alone cannot explain the luminosity of this excess light, accounting for only $\sim 35\%$ of the excess in the NIR profile. Furthermore, at the *I* band, no significant dust emission would be expected at all. Two additional clues paint a complicated picture. First, the color in the central $0''.2$ is somewhat bluer in the *HST F547M − F814W* images (Figure 2) and has compact UV emission (Maoz et al. 2005), both suggestive of the presence of young stars. Second, the stars in this area appear to be counter-rotating relative to the NSC and galaxy (see Section 4.1). Thus, the central excess appears to result from a combination of hot-dust emission, younger stars, and perhaps AGN continuum emission in the optical and UV.

In summary, we find evidence for three components at the center of NGC 404:

1. a bulge with Sérsic $n \sim 2.5$ and effective radius of 640 pc that dominates the light between $1''$ and $80''$ (and beyond);
2. an NSC which dominates the light in the central arcsecond (15 pc); and
3. a central excess at $r < 0''.2$. This excess appears to result from the combination of hot dust, young stars, and perhaps AGN continuum emission.

Within the central $1''$ in the *I* band (roughly the area included in the MMT spectrum analyzed in Section 5), $\sim 55\%$ of the light comes from the NSC, 29% from the underlying bulge, and 16% from the central excess.

The isophotes in the ACS *F814W* data at $10''-80''$ have a position angle (P.A.) of $\sim 80°$ and an ellipticity of ~ 0.08. This matches well with the morphology of the H I disk on a large scale; del Río et al. (2004) find an H I inclination of $\sim 10°$ and a P.A. of about $\sim 80°$ for radii between $100''-300''$. Due to dust absorption, the clearest picture of the inner arcsecond of NGC 404 comes from the NIFS *K*-band image. As can be seen from the contours in Figure 2, the P.A. at $r < 0''.25$ is $60°-70°$. The P.A. then abruptly changes to $25°$ at $r = 0''.3$ and gradually increases to the large-scale P.A. of $80°$ by $\sim 1''$. The ellipticity decreases from ~ 0.2 near the center to 0.07 at $1''$. These changes fit well with our picture of three distinct components, each having their own distinct morphology.

3.1. A Hot-dust Component

Within the central $0''.2$, the NIFS spectra show a significant spectral flattening and a reduction in the depths of the CO lines by about 10%. A comparison of the central spectrum to single stellar population models from Maraston (2005) shows that its spectral slope is flatter/redder than any stellar population models. Furthermore, the younger stellar populations expected in the central excess should have a somewhat bluer, not redder, continuum. This redder continuum suggests two possibilities: (1) strong dust absorption or (2) emission from hot dust.

We rule out dust absorption as a possibility because the required dust absorption to flatten the spectrum is $A_V \sim 6$ mag assuming the reddening law from Cardelli et al. (1989). The $F547M - F814W$ shows that the nucleus is actually *bluer* than the surrounding areas ($F547M - F814W \sim 0.8$). Furthermore, the area to the west of the nucleus appears unreddened with $F547W - F814W \sim 0.95$, consistent with the expected color of the stellar population based on spectroscopic fits (see Section 5.2), while the eastern half of the nucleus is at most 0.8 mag redder in $F547M - F814W$ (approximately $V-I$). This suggests a maximum extinction in the region around the nucleus of $A_V \sim 2$.

Therefore, hot dust appears to be the cause of the flattened continuum in the central pixels. Hot dust is a common feature in Seyfert nuclei at NIR wavelengths, and is typically found to have temperatures of 800–1300 K (Alonso-Herrero et al. 1996; Winge et al. 2000; Riffel et al. 2009). Studies of Seyfert galaxies with NICMOS by Quillen et al. (2000, 2001) show that the hot-dust component is frequently unresolved and variable on months to year timescales. The presence of hot-dust components in LINER galaxies appears to be unstudied.

We fit the contribution and temperature of this hot-dust emission by assuming that the central spectrum is made up of an NSC spectrum drawn from an annulus of $0''.5-1''.0$ plus a pure blackbody spectrum. As shown in Figure 4, the central spectrum ($r \leqslant 0''.05$) is best fitted by a dust temperature of 950 K, contributing about 20% of the light. The residuals between the
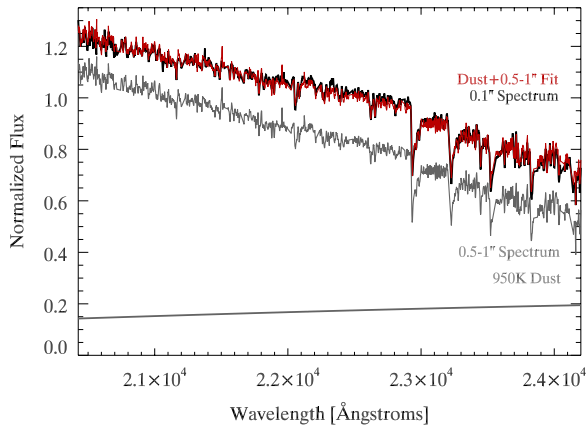
Figure 4. Fit of the central NIFS spectrum of NGC 404 to a model including emission from hot dust. The black line shows the central spectrum, with the overplotted line showing the best fit. This fit consists of a template stellar spectrum taken from an annulus of radius $0''.5$–$1''.0$, plus a blackbody of temperature 950 K (shown in gray). Note that emission lines were excluded from the fit and the plot.

(A color version of this figure is available in the online journal.)

Figure 5. Surface brightness profile of the NICMOS *F160W* observations (NIC2 in red and NIC3 in orange), 2MASS *H*-band (dashed), and NIFS *K*-band observations scaled to match the *F160W* NICMOS observations at $r > 1''$. The dashed line shows the NIFS observations after correction for dust emission.

(A color version of this figure is available in the online journal.)

central spectra and the model have a standard deviation of 1.4% across the band, and the fit completely eliminates the difference in spectral slopes between the annular and the central spectrum.

Fitting a spectrum in radial annuli, we find no evidence for dust emission beyond $0''.3$ from the nucleus. Assuming a uniform dust temperature of 950 K, we calculated the contribution of dust in each individual spaxel. Using this, we correct the *K*-band image for the hot-dust contribution. We use the dust-corrected *K*-band image and central position for all our subsequent analysis. The dust emission accounts for only ∼35% of the central excess in the NIR, as is shown with the blue points in the right panel of Figure 3.

The dust emission is slightly offset to the NE of the photocenter. This offset is in the direction of the dust absorption clearly seen on larger scales to the east of the cluster in the *HST* color image (Figure 2). The corrected image has a photocenter offset by about a half-pixel from the uncorrected image, while the dust emission is offset by ∼1.5 pixels from the corrected photocenter. The small shift in the photocenter reduces the asymmetry in the velocity field, moving the photocenter to the center of the central counter-rotation (see Section 4.1). As found in other AGNs, the hot-dust component is unresolved, with a measured FWHM of $0''.14$ (single-Gaussian PSF fits give an FWHM of ∼$0''.18$ for our NIFS data).

The total dust emission in the *K* band has a magnitude of $K \sim 15.4$ which translates to a flux of 1.3×10^{-13} erg s^{-1} cm^{-2} and a luminosity of 1.4×10^{38} erg s^{-1}. Assuming the hot-dust emission is the result of accretion onto a BH of ∼$10^5 M_\odot$ (Section 6), this suggests $L_{bol}/L_{Edd} \gtrsim 10^{-5}$; typical LINERS have $L_{bol}/L_{Edd} \sim 3 \times 10^{-5}$ (Ho 2004). The hot-dust luminosity is somewhat larger than the [O III] luminosity (assuming $D = 3.06$ Mpc) of 2×10^{37} erg s^{-1} (Ho et al. 1997) and the possible hard X-ray component with 2–10 keV luminosity of ∼3×10^{37} erg s^{-1} noted by Terashima et al. (2002). The 1.6 μm dust emission, [O III], and hard X-ray luminosities of Seyfert galaxies are discussed in detail by Quillen et al. (2001). Although the luminosities presented here are much lower than those in their sample (as would be expected for a system with a lower accretion rate), the relative luminosities in these three bands fall within the scatter of their data suggesting a comparable spectral energy distribution (SED).
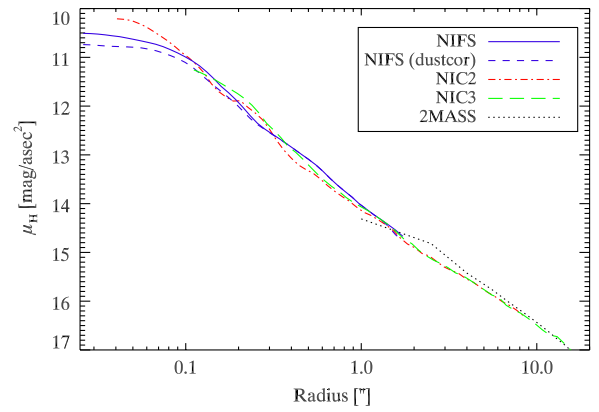
We also find tentative evidence for variability in the dust emission between our NIFS images taken in 2008 and *HST* NICMOS images taken in 1998. This variability may be expected given the variability in the nuclear UV flux reported by Maoz et al. (2005). They find that the flux at 2500 Å decreases by a factor of ∼3 between 1994 and 2002. However, this comparison is based on observations by three different cameras, the earliest of which was a $0''.86$ aperture spectrum; thus, spatial resolution of the UV variability is not possible.

Figure 5 shows a comparison of the SB profiles of all the NIR data, with the NIFS *K*-band image scaled to fit the SB profile of the NICMOS *F160W* images at $r > 1''$. Within the central $0''.2$, the scaled NIFS luminosity is clearly fainter than the NIC2 image. This change in brightness could be explained by a bluer stellar population within the central excess, but the effect is much larger than expected—the $F547M - F814W$ image shows a change of $\Delta(F547M - F814W) \sim 0.1$ mag between the center and the NSC at larger radii, implying a $\Delta(H - K) < 0.1$. However, the observed $\Delta(H - K) = 0.4$ after attempting to correct both the NIC2 image and the NIFS dust-subtracted image for the effects of the PSF. Using the original NIFS image (without dust subtraction), we still get $\Delta(H - K) = 0.3$. We suggest that this large $\Delta(H - K)$ may result from variable dust emission, with the NIC2 observations being taken at an earlier epoch when the dust emission was more prominent. Multi-epoch *HST* observations of the nucleus in the UV and NIR using the same instrument will be extremely useful for verifying a possible variable AGN contribution and constraining its SED.

3.2. NIR Emission-line Excitation

In this section, we discuss the emission lines observed in the Gemini/NIFS *K*-band spectrum. We find that they imply that the emission originates in dense molecular gas with line ratios typical of those observed in known AGNs.

To obtain estimates for line emission in the NGC 404 nucleus, we summed together flux-calibrated integrated spectra from our NIFS data with radii ranging between 1 and 25 pixels. We then used both the Wallace & Hinkle (1996) and Winge et al. (2009) templates to fit the stellar continuum from 20200 Å to 24100 Å excluding the parts of the spectrum near known emission lines. Subtracting this continuum off left us with a pure emission spectrum. We measured numerous H_2 emission lines as well as
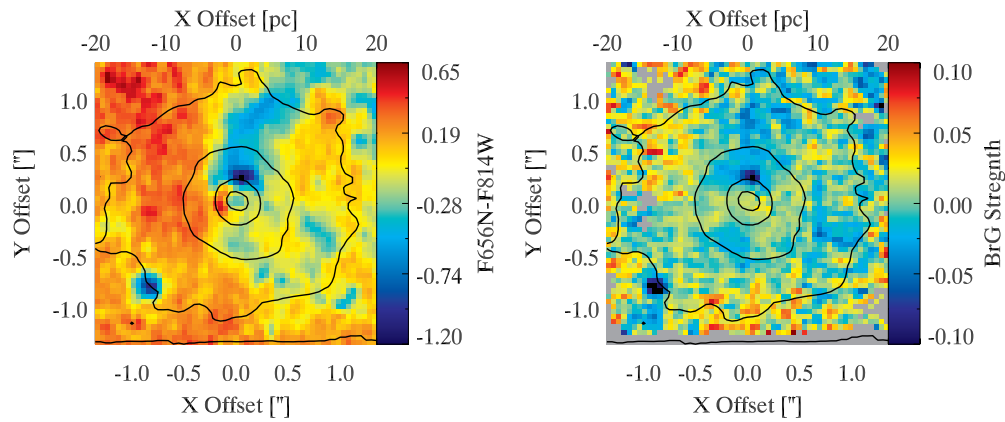
Figure 6. Left: WFPC2 $F656N - F814W$ map of the nuclear region. Negative values are areas with strong Hα emission. Right: Brγ emission line map. Negative values mean strong Brγ emission, while positive values result from Brγ absorption. Contours and orientation are identical to those in Figure 2.

(A color version of this figure is available in the online journal.)

Brγ emission. The only observable coronal line commonly seen in AGNs is [Ca VIII], which falls directly on a CO band head; a 3σ upper limit of 3.6×10^{-17} erg s^{-1} cm^{-2} was placed on this line.

Detected H$_2$ lines (and their vacuum wavelengths) included 1–0 S(2) (20337.6 Å), 2–1 S(3) (20734.7 Å), 1–0 S(1) (21218.3 Å), 2–1 S(2) (21542.1 Å), 1–0 S(0) (22232.9 Å), 2–1 S(1) (22477.2 Å), and 1–0 Q(1) (24065.9 Å). Line ratios of these lines can be used to determine the excitation mechanisms of the gas. In particular, the ratio of the 2–1 S(1) and 1–0 S(1) lines is between 0.11 and 0.16 with smaller values at larger radii. These values are indicative of thermal excitation from shocks or X-ray photons in a dense cloud ($n \gtrsim 10^4$ cm^{-3}), while fluorescent emission in a low-density medium has a higher 2–1 S(1)/1–0 S(1) of $\sim$0.55 (e.g., Mouri 1994). The observed ratio is typical of those observed in other AGNs (e.g., Reunanen et al. 2002; Riffel et al. 2008; Storchi-Bergmann et al. 2009).

The rotational and vibrational temperatures can be estimated from ratios of H$_2$ lines; using the relation from Reunanen et al. (2002) $T_{\rm vib} = 5600/\ln(F(1–0S(1))/F(2–1S(1))*1.355)$, we find $T_{\rm vib} = 2340 \pm 160$ K within a 1$''$ radius aperture. Similarly, the rotational temperature can be determined using the relation $T_{\rm rot} = -1113/\ln(F(1–0S(2))/F(1–0S(0))*0.323)$ (Reunanen et al. 2002) which gives a somewhat lower temperature of $T_{\rm rot} = 1640 \pm 360$ K within a 1$''$ aperture. The higher vibrational temperature may be indicative of some contribution of fluorescence (e.g., Riffel et al. 2008).

Unfortunately, the Brγ emission-line flux cannot be accurately estimated due to uncorrected telluric absorption in the vicinity of the Brγ line. However, the distribution of Brγ flux is much patchier than the H$_2$ (see Figure 6) suggesting different sites for the two types of emission. Note that in starbursting galaxies, the Brγ is stronger than the H$_2$ 1–0 S(1) line (Rodríguez-Ardila et al. 2004), a possibility which is clearly excluded by our data (see Figure 1). This again is consistent with emission originating due to thermal excitation in dense gas as suggested by the H$_2$ 2–1 S(1)/1–0 S(1) ratio.

The distribution of Brγ and Hα visible in Figure 6 emission is primarily concentrated in two clumps, one just to the north of the nucleus and one $\sim$1$''$ to the SE. These are likely the sites of the most recent star formation in the nucleus. In Section 5, we find a total young stellar mass at ages $\lesssim$ 10 Myr of $\sim 10^4\ M_\odot$. The central excess has bluer optical colors and UV emission but lacks strong Hα or Brγ emission, suggesting that the

young stars there have an age of $\gtrsim$10 Myr (Gogarten et al. 2009).

4. KINEMATICS

Our NIFS data enable us to derive kinematics for both the absorption lines, using the CO band heads from 22900 to 24000 Å and the strongest of the H$_2$ lines at 21218 Å.

4.1. Stellar Kinematics

The velocity and dispersion across the NIFS field of view (FOV) are shown in Figure 7. At radii of $\sim$1$''$, we see a blue shift to the west and a red shift to the east, rotation that is in the same direction as the H I rotation seen at larger radii (del Río et al. 2004). At $r \lesssim 0\rlap{.}''2$, there appears to be modest counter-rotation. An alternative view of the velocity field is seen in Figure 8 which shows the LOSVD profile along a P.A. = 80°. The error bars in the velocity range from <1 km s^{-1} near the center to $\sim$5 km s^{-1} at large radii. The counter-rotation seen in the central excess (at $r < 0\rlap{.}''2$) is clearly significant. However, given the nearly face-on orientation of the larger scale of the galaxy, this counter-rotation does not necessarily imply a large ($>$90°) difference in the angle of the rotation axes of the two stellar components.

To quantify the P.A. and amplitude of the rotation as a function of radius, we used the kinemetry program of Krajnović et al. (2006). This kinemetry program uses a generalized version of ellipse fitting to analyze and quantify the velocity map or other higher order moments of the LOSVD. We present the results of the kinemetry analysis of the velocity maps in Figure 9, showing the systemic velocity, P.A., and rotation speed as a function of radius. We limited the axial ratio to between 0.8 and 0.95 (consistent with our ellipse fits to the K-band image), and fixed the center to the photocenter of the dust-corrected K-band image. We find an amplitude for the central counter-rotation of 3.3 km s^{-1} (shown in triangles in Figure 9), while the rotation at larger radii has a maximum rotation amplitude of 8.4 km s^{-1} at 1$\rlap{.}''$2. The P.A.s of the counter-rotation and rotation at larger radii are quite similar, with values of 80°–90° (east of north). Our observed rotation is at a similar P.A. to the H I gas, which has a rotation axis of 70°–90° from 100$''$–300$''$ (del Río et al. 2004). The maximum observed rotation velocity of the H I gas is $\sim$45 km s^{-1}. Recent observations of the stellar kinematics
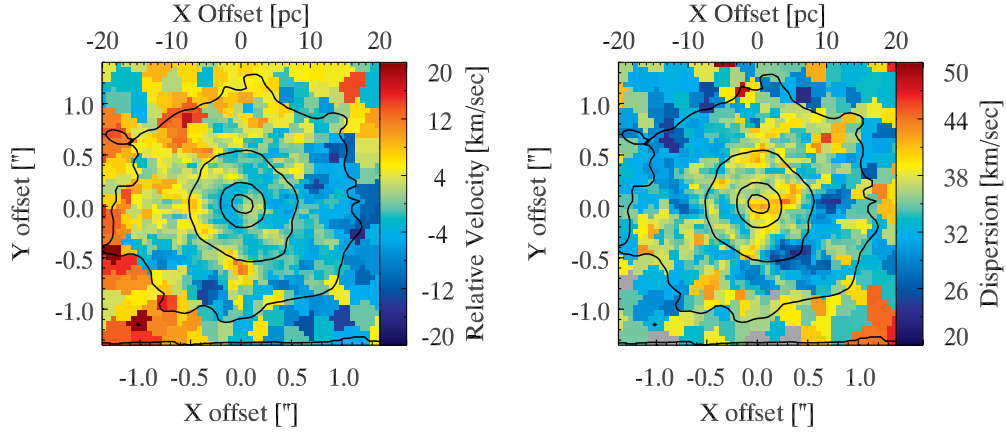
Figure 7. Velocity and dispersion of the stellar component derived from the CO band head. Contours show contours of the *K*-band image with contours separated by a magnitude in SB (as in Figure 2). Radial velocities are shown relative to the central velocity of -58.9 km s^{-1}.

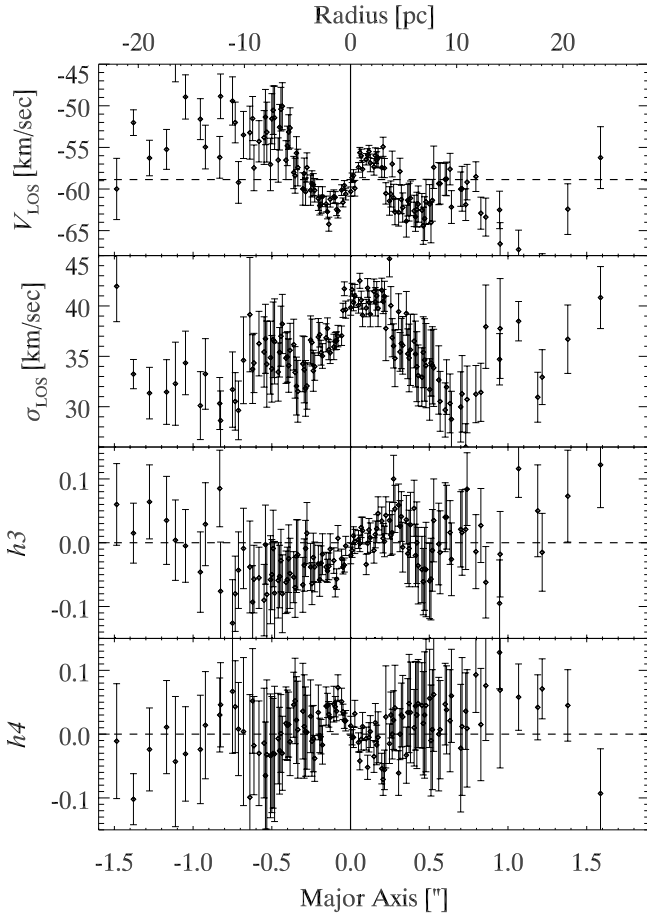(A color version of this figure is available in the online journal.)

Figure 8. LOSVD along the major axis of the innermost component at P.A. = $80°$. Panels show the radial velocity, LOS dispersion, and $h3$ and $h4$ components of the LOSVD (from top to bottom). Bin centers falling within $0\rlap{.}''1$ of the major axis are plotted.
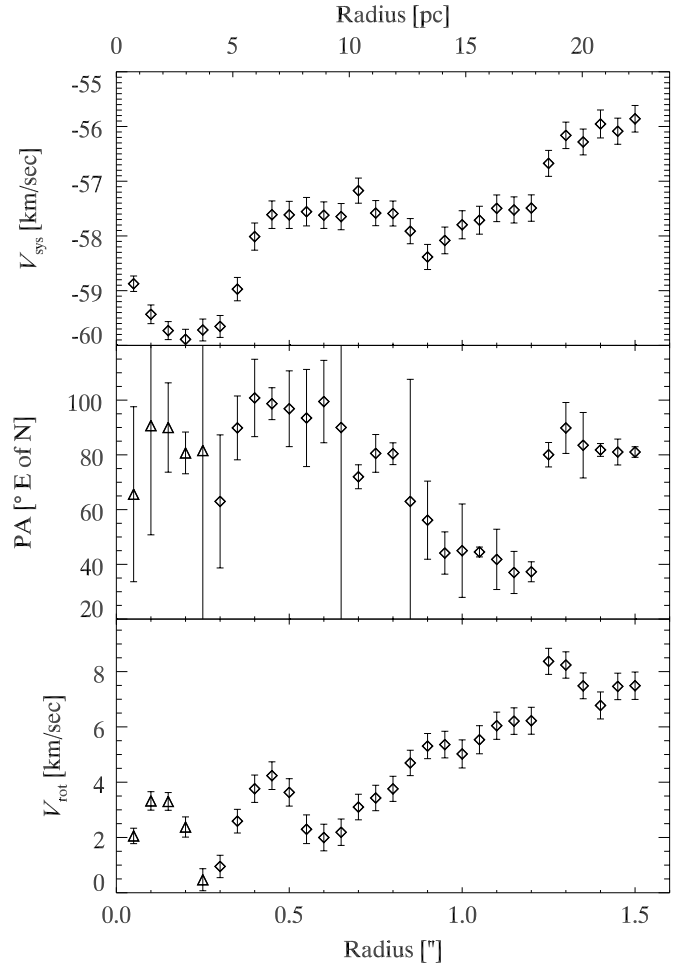

Figure 9. Results of kinemetric analysis of the stellar velocity field as a function of radius. Top: the systemic velocity, middle: the P.A., bottom: the amplitude of rotation. Triangles in bottom two panels indicate counter-rotation.

along the major axis by Bouchard et al. (2010) suggest that increasing counter-rotation relative to the H I is seen between radii of $1''$–$20''$, with rotation in the sense of the H I again taking over at larger radii. Clearly, large-scale IFU kinematics of this galaxy would be very interesting.

A radial profile of the stellar dispersion is shown in Figure 10 for bins with uncertainties in the dispersion of <10 km s^{-1}. While the scatter of values is large at most radii, the velocity

dispersion clearly declines from $\sim$40 km s^{-1} at the center to a mean value of $\sim$33 km s^{-1} at $0\rlap{.}''6$. Our dispersion values are consistent with the 40 ± 3 km s^{-1} determined by Barth et al. (2002) for the NGC 404 center using the calcium triplet. Dynamical modeling based on the stellar kinematics is detailed in Section 6.1.
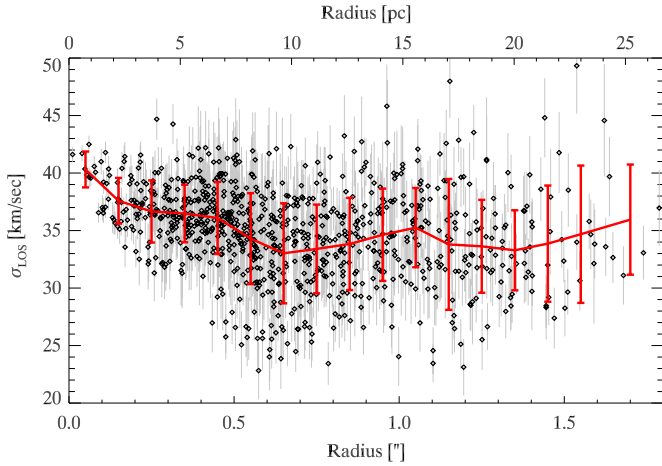
Figure 10. LOS dispersion values as a function of radius for all data points with dispersion errors less than 10 km s^{-1}. Error bars on individual points can be seen in light gray. The thick line shows a binned average and standard deviation as a function of radius.

(A color version of this figure is available in the online journal.)

Figure 12. Rotation velocity (black line) and dispersion (blue dashed line) derived from the H$_2$ 21218 Å line using the kinemetry program of Krajnović et al. (2006).

(A color version of this figure is available in the online journal.)

4.2. H$_2$ Gas Kinematics and Morphology

The H$_2$ gas kinematics and morphology were derived by fitting the 21218 Å 1–0 S(1) emission line, the strongest of the H$_2$ emission lines in the K band. In each spaxel, we fit this line with a Gaussian to derive a flux, radial velocity, and velocity dispersion (after correction for the instrumental resolution). The results of these fits are shown in Figure 11. The physical condition of this gas is discussed more in Section 3.2. We note that the mass of luminous excited H$_2$ gas is very small ($< 1 \, M_\odot$) and although it likely tracers a larger mass of colder molecular gas, this gas is not expected to be dynamically significant in the nucleus (Wiklind & Henkel 1990).

The H$_2$ emission peaks slightly to the SW of the continuum emission, $\sim 0\farcs07$ from the centroid of the dust-emission-corrected continuum (see white contours in Figure 11). The FWHM of the distribution is $\sim 0\farcs4$ (6 pc). At $r \lesssim 0\farcs3$, it is elongated ($q \sim 0.6$) with P.A. $\sim 25°$.

The H$_2$ gas velocity field provides a significant contrast with the stellar velocity field. It shows a clear rotation signature at a P.A. nearly orthogonal to the stellar rotation. Using the
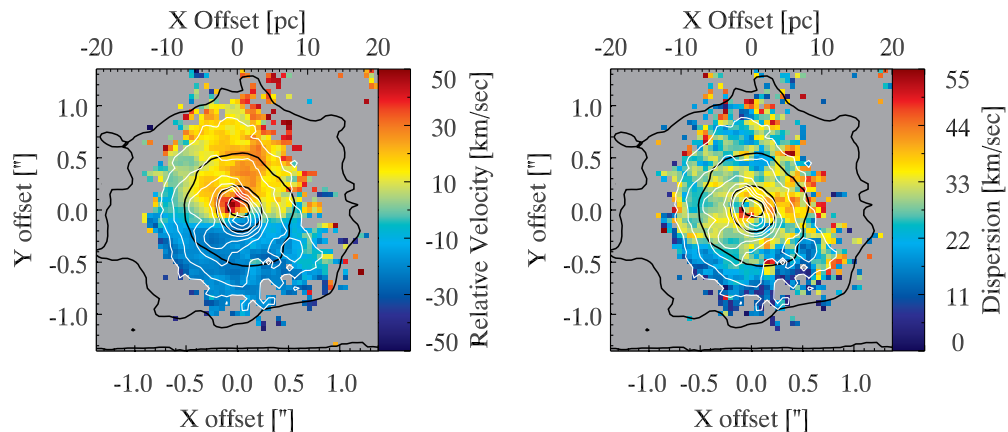
kinematric analysis program (Krajnović et al. 2006), we find a kinematic P.A. of $\sim 15°$ out to $0\farcs2$, which then twists to P.A. ~ -10 at larger radii. A radial profile of the rotation velocity and dispersion are shown in Figure 12. The rotation peaks at $r \sim 0\farcs15$ (2.2 pc) with an amplitude of 36 km s^{-1}. Beyond $0\farcs3$, the rotation flattens out to an amplitude of 20–25 km s^{-1}. The central dispersion ($r = 0\farcs05$) is 39 km s^{-1}, which likely includes unresolved rotation. At $r = 0\farcs1$ it drops to 33 km s^{-1}, then slowly declines to ~ 25 km s^{-1} at larger radii. Dynamical modeling of the gas kinematics is presented in Section 6.2.

The axial ratio of the intensity distribution and our gas dynamical model suggest an inclination of $\sim 30°$ at $r < 0\farcs3$, with smaller inclinations at larger radii. Assuming this geometry, the H$_2$ disk appears to be rotation dominated at all radii with $V_{\rm rot}/\sigma \sim 2$ near the center. H$_2$ emission-line disks are commonly observed in nearby AGNs (Neumayer et al. 2007; Riffel et al. 2008; Hicks et al. 2009), although the sizes of these disks are typically much larger than that in NGC 404. For instance, in the Hicks et al. (2009) sample of 11 nearby AGNs, they find H$_2$ disks traced by the 21218 Å line with half-width

Figure 11. Velocity and dispersion of the molecular hydrogen data determined from the 1–0 S(1) line at 21218 Å. Black contours indicate the SB of the K-band image with contours separated by a magnitude in SB. White contours show the H$_2$ total intensity 5%, 10%, 20%, 30%, 40%, 50%, 70%, and 90% of the peak. Radial velocities are shown relative to the central stellar radial velocity (-58.9 km s^{-1}).

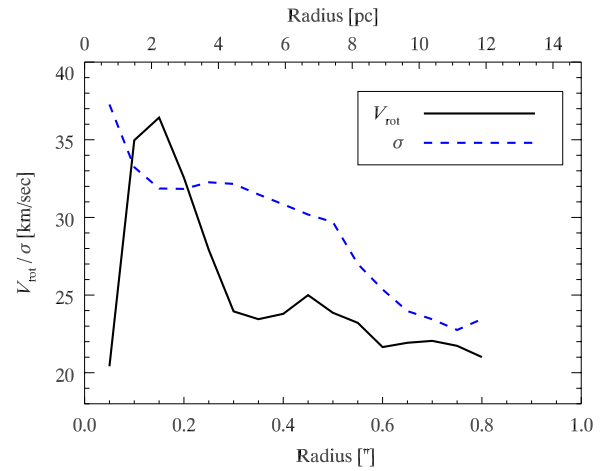(A color version of this figure is available in the online journal.)

at half-maximum values ranging from 7 to 77 pc (versus 3 pc in NGC 404). Most of these disks have V_{rot}/σ values of ~1, although a couple have $V_{rot}/\sigma > 2$ at larger radii.

5. STELLAR POPULATIONS

In this section, we use the optical spectrum of the NGC 404 NSC to constrain its formation history. We first use the optical emission lines to constrain the reddening and derive a maximum current star formation rate (SFR) of $1.0 \times 10^{-3} M_\odot$ yr^{-1}. Fits to the absorption line spectrum show that the nucleus has a range of stellar ages, with stars ~1 Gyr in age contributing more than half the light of the spectrum. Next, we consider the range in mass-to-light ratios (M/Ls) allowed by the stellar population fits. Finally, we show that the bulge has a distinctly older stellar population than the nucleus.

5.1. Optical Emission-line Information

Before discussing our fits to the optical absorption-line spectrum, we first use the optical emission lines to estimate the reddening, current metallicity, and SFR. We note again that our line fluxes and ratios agree very well with those in Ho et al. (1997).

After correcting for the underlying stellar population using our population fits described below, we find a Balmer decrement ($F(H\alpha)/F(H\beta)$) of 3.59. For an AGN, the expected Balmer decrement is 3.1 while for an H II region it is 2.85 (Osterbrock 1989). Given the ambiguous nature of the nuclear emission, this suggests extinctions of $A_V = 0.43$–0.73. As noted in Section 3.1, the $F547W - F814W$ color map indicates extinctions of $A_V \lesssim 2$ covering about half the nucleus; thus, these Balmer decrement extinction values seem reasonable. We note that the patchy distribution of the Hα emission (see Figure 6) is significantly different from the stellar light distribution; thus the Balmer decrement extinction may not exactly match the extinction of the stellar light.

If we assume that the emission is primarily powered by star formation, then we can estimate the metallicity based on strong-line indicators. Using the metallicity calibration of the [O II]/[N II] ratio by Kewley & Dopita (2002), we find a metallicity of $12 + \log(O/H) = 8.84$, roughly solar. We can also estimate the gas-phase metallicity from the Tremonti et al. (2004) metallicity–luminosity relationship; assuming $M_B \sim -16.75$, (using values from Tikhonov et al. 2003), we get a metallicity $12 + \log(O/H) = 8.33$. These results suggest a solar or slightly subsolar current gas-phase metallicity.

Finally, we can place an upper limit on the current SFR in the nucleus using the Hα luminosity. Correcting for extinction, we get an Hα flux of 10.8×10^{-14} erg s^{-1} cm^{-2} corresponding to $L_{H\alpha} = 1.2 \times 10^{38}$ erg s^{-1}. This gives an upper limit to the current SFR of $1.0 \times 10^{-3} M_\odot$ yr^{-1} using the Kennicutt (1998) relation. The value is an upper limit as some of the Hα flux may originate from AGN activity. The radio continuum detection of 3 mJy at 1.4 cm by del Río et al. (2004) implies an SFR of ~$2 \times 10^{-4} M_\odot$ yr^{-1} if it is the result of recent star formation.

The UV spectra of Maoz et al. (1998) in a 0″.86 aperture also suggest the presence of O stars in the nucleus. We correct their estimate of the number of O stars to a distance of 3 Mpc and for extinction of $A_V = 0.5$–1.0. This gives a range of 17–170 O stars, suggesting a total stellar mass of 4000–40000 $M_\odot$ assuming a Kroupa et al. (1993) initial mass function (IMF). The low ends of these estimates are consistent with the $10^{3-4} M_\odot$ of recent stars implied by the Hα and radio SFRs assuming formation over the last ~10 Myr.

5.2. Nuclear Cluster Stellar Populations

In this section, we fit the integrated nuclear optical spectrum to determine the stellar populations of the NSC. We find that stars with a range of ages are present, but that stars 1–3 Gyr make up $\gtrsim$50% ($6 \times 10^5 M_\odot$) of the NSC mass. This dominant population has a solar or slightly subsolar metallicity ($[Z] = -0.4$). About $10^4 M_\odot$ of young stars are also present. These results are consistent with other studies of the NGC 404 nucleus (Cid Fernandes et al. 2004; Bouchard et al. 2010).

We fit the flux-calibrated spectrum between 3740 and 6200 Å, avoiding the second-order UV contamination at wavelengths above 6200 Å. For stellar population models we use both (1) the Bruzual & Charlot (2003) models (BC03) which are based on Padova stellar models (Bertelli et al. 1994; Girardi et al. 2000) and the STELIB library of stellar spectra (Le Borgne et al. 2003), and (2) the updated version of the BC03 models incorporating the asymptotic giant branch (AGB) models of Marigo & Girardi (2007) and Marigo et al. (2008) obtained from Stéphane Charlot, which we will refer to as CB07 models. These models provide spectra for single age simple stellar populations (SSPs) over a finely spaced age grid and at metallicities of $Z = 0.0001, 0.0004, 0.004, 0.008, 0.02,$ and 0.05 at a spectral resolution similar to our observations. We find that typically the CB07 models more accurately describe the data; they differ from the BC03 models by up to 10% across the wavelength range we are considering here.

To remove known problems in the wavelength calibration of the STELIB library (Koleva et al. 2008) and any wavelength issues in our own spectrum, we determined the relative velocity between our spectrum and the SSP models every 100 Å. Variations of up to ± 35 km s^{-1} around the systemic velocity were found and corrected. We also made a flux calibration correction of $\leqslant 3\%$ across the spectrum that was determined from residuals of our fits to the nuclear clusters in NGC 404, NGC 205, M33, and NGC 2403—this is described in more detail below. We fit the models to our spectrum using Christy Tremonti's *simplefit* program (Tremonti et al. 2004), which uses a Levenberg–Marquardt algorithm to perform a χ^2 minimization to find the best-fit extinction (using the prescription of Charlot & Fall 2000) and scalings of the input model spectra. The code excludes the regions around expected emission lines from the fit.

We started our fitting by considering just single age stellar populations. Over the full range of 3740–6200 Å, the best-fitting SSP is the CB07 model with age = 1.14 Gyr, $Z = 0.004$, and $A_V = 0.85$ mag. The reduced χ^2 is 21.8 corresponding to typical residuals of 3%. This fit is shown in Figure 13 as the blue line. The residuals are dominated by a mismatch between the large-scale shape of the nuclear cluster continuum with the SSP model. To mitigate these effects and get a better sense of the metallicity, we also tried fitting just the metal-line-rich region from 5050 to 5700 Å. The best fit is again a CB07 model with an age of 1.14 Gyr, but with $Z = 0.008$ and $A_V = 0.91$. This metallicity and reddening are quite similar to the values expected based on the emission lines and the mass–metallicity relationship.

Previous studies have found significant evidence for multiple stellar populations in NSCs (Long et al. 2002; Rossa et al. 2006; Walcher et al. 2006; Seth et al. 2006; Siegel et al. 2007). While most of these studies have focused on spiral galaxies, there is also direct evidence that the NGC 404 NSC contains multiple stellar populations; Maoz et al. (1998) find evidence for massive O stars, suggesting a population with age $\lesssim$ 10 Myr, while
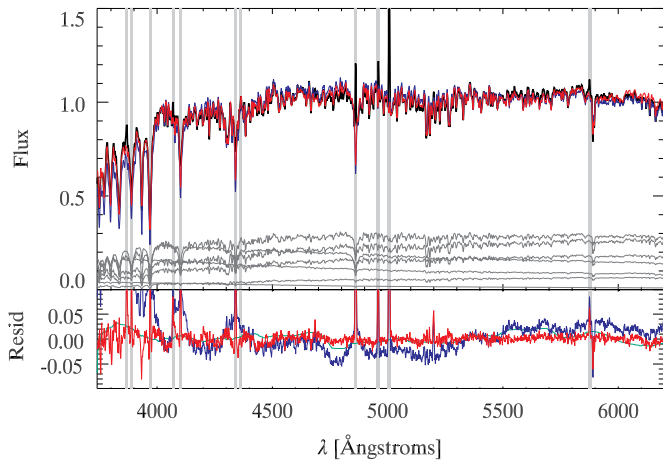
Figure 13. Top panel: normalized spectrum of the NGC 404 nucleus (black) with the best-fitting single age (blue) and multi-age (red) fits to the spectrum. Vertical lines show emission-line regions that were excluded from the fit. Gray spectra indicate the different aged SSPs contributing to the multi-age fit. Bottom panel: residuals of the best-fit single age (blue) and multi-age (red) fits. Also shown is the flux calibration correction described in the text.

(A color version of this figure is available in the online journal.)

based on the color of the nucleus and its spectrum, older stars are clearly present as well. Also, as discussed in Section 3.1, we expect contamination of ∼30% from the bulge in our MMT spectrum.

We tried a number of approaches to our multi-age fits. All of these involved fitting a small subsample (∼10) of the SSPs with ages ranging from 1 Myr to 20 Gyr (see Walcher et al. 2006; Koleva et al. 2008, for a more complete discussion of stellar population synthesis). We tried three types of models with both the CB07 and BC03 spectra:

1. Single-metallicity models using the 10 default ages in the *simplefit* code (5, 25, 101, 286, 640, 904, 1434, 2500, 5000, and 10000 Myr) or the 14 age bins used by Walcher et al. (2006) (1, 3, 6, 10, 30, 57, 101, 286, 570, 1015, 3000, 6000, 10000, and 20000 Myr).

2. Inspired by observations of the Sgr dSph nucleus (aka M54; Monaco et al. 2005; Siegel et al. 2007), we also tried fitting models with chemical evolution from low metallicity ($Z = 0.0004/[M/H] = −1.7$) at old ages (13 Gyr) to solar metallicity for young ages (following Figure 2 from Siegel et al. 2007). Specifically, we used a model with $Z = 0.02$ at ages of 1, 10, 50, 101, 286, 570, 1015, and 2500 Myr plus $Z = 0.008$ models at 5000 and 10000 Myr and $Z = 0.0004$ models at 13000 Myr.

3. Assuming a continuous or exponential star formation history (SFH) with chemical evolution similar to the previous item.

Of all the single-metallicity models (model 1), the best fit is obtained with the CB07 spectra using the default ages with $Z = 0.008$ yielding a reduced χ^2 of 4.3 and typical residuals of 1%.

This is a vast improvement over the best-fit SSP model. The fit is dominated by intermediate age stars, with 72% of the light in the 1.434 Gyr SSP. Many other models also produce nearly as good fits as this one including models with solar and supersolar metallicity.

All the best-fitting ($\chi^2_{\rm red} < 5$) models have fairly similar age distributions with 50%–85% of the light coming from ages between 600 and 3000 Myr, 5%–6% of the light coming from ages <10 Myr, and 0%–25% of the light coming from ages >5 Gyr. The A_V values range from 0.84 to 1.16 and the implied $V−I$ colors range from 0.84 to 1.04.

The spectrum is not well fitted by a constant SFH (model 3), giving a reduced χ^2 of 22. The constant SFH clearly has too many young stars, with the continuum mismatched in a way that cannot be compensated for by the reddening. We note that a constant SFH does provide good fits to the spectra of nuclei in many late-type galaxies (Seth et al. 2006; Walcher et al. 2006). An exponentially declining SFH with a timescale of ∼8 Gyr does a better job of matching the overall continuum of the observations, but still yields a reduced χ^2 double that of our best-fitting models.

The best-fit model is obtained from model 2, which contains metallicity evolution. The reduced χ^2 of the best fit is 4.23, slightly better than any of the single-metallicity models. This model is shown in red in Figure 13 with the individual SSP components shown in gray in the top panel. The best-fit model has significant contributions from many of the individual ages; these are shown in Table 3. It is once again dominated by 1–3 Gyr old stars, which make up half the mass of the NSC. This appears to be a robust result, with all our best-fit models containing a similar result. The luminosity-weighted mean age is 2.3 Gyr and the mass-weighted mean age is 4.3 Gyr. The best-fit A_V is 0.88 and the M/Ls are 0.89, 0.73, and 0.34 in the V, I, and H bands. NGC 404 does not seem to have a dominant old metal-poor population like that seen in M54 (Monaco et al. 2005). From the M/L analysis presented in Section 5.3, we find that the maximum contribution for an old (13 Gyr) metal-poor ($Z = 0.0004$) population that keeps the reduced χ^2 below 5 is ∼17% of the luminosity in the V band and ∼35% of the total mass.

We can compare our best-fit model to other observed properties of the nucleus. The integrated colors of the best-fit model are $I − H = 1.59$ and $V − I = 0.96$. An estimate of the $I − H \sim 1.7$ (Table 2) comes from the SB profiles, while the $F547W − F814W \sim V − I \sim 0.95$ comes from the unreddened west portion of the nucleus in Figure 2. Both of these quantities need to be corrected for foreground extinctions of $E(I − H)$ and $E(V − I)$ of 0.06 and 0.08 mag; after this correction, the measured integrated colors agree with the best-fit spectral synthesis model to within 10%.

The best-fit model also suggests that the young stars (⩽10 Myr) make up 6%/0.2% of the light/mass in the H band and 8%/0.3% of the light/mass in the I band. This gives a mass of about $1.1 \times 10^4\ M_\odot$ in young stars, in very good agreement with Hα SFR integrated over 10 Myr and the estimates from the UV spectra (see the discussion in Section 5.1; Maoz et al. 1998).

Table 3
Best-fit NSC Stellar Population Model

Age (Myr)	1	10	50	101	286	570	1015	2500	5000	10 000	13 000
Z	0.02	0.02	0.02	0.02	0.02	0.02	0.02	0.02	0.008	0.008	0.0004
Light fraction	0.013	0.090	0.000	0.000	0.157	0.000	0.277	0.239	0.166	0.058	0.000
Mass fraction	0.000	0.003	0.000	0.000	0.035	0.000	0.152	0.317	0.316	0.177	0.000

Finally, we compared the spectrum of NGC 404 to other NSCs for which we took spectra on the same night, including M33, NGC 205, NGC 2403, and NGC 2976. Both M33 and NGC 205 do better than any single stellar population model at matching the NGC 404 spectrum, with reduced χ^2 values of 9.3 and 15.0. The stellar populations in the M33 nucleus have been previously discussed by Long et al. (2002). They find that the spectrum requires a large contribution of stars with an age of ~1 Gyr and a lesser contribution of stars at 40 Myr. This dominant 1 Gyr population is consistent with our findings above. In our initial fits of these NSCs, we noted that the residual pattern was quite similar regardless of the details of the fit, with the most dramatic feature being a change of a few percent between 4700 and 4800 Å. Our flux calibration errors are expected to be at this level based on the residuals from the flux calibrators. Given the similarities of the residuals in all of the nuclear spectra, we medianed the best-fit model 1 residual spectra from NGC 205, M33, NGC 404, and NGC 2403, then smoothed it and used it as a correction to our flux calibration. The correction is shown as the green line in the residual plot in Figure 13. This change improved the χ^2 of the single stellar population and multi-age fits substantially at all metallicities but had little effect on the best-fit parameters.

The stellar population of NGC 404 has been previously studied by Cid Fernandes et al. (2004) who analyzed the blue spectrum (3400–5500 Å) of the NGC 404 nucleus as part of a study of a large number of LINER nuclei. Using empirical templates of five nuclei ranging from young to old they find a best fit for NGC 404 of 78.5% of light in an intermediate age template (for which they used a spectrum of NGC 205) and 21.5% from old templates, with an A_V of 0.90 and residuals of 6.6%; this residual is much larger than that for our fits (with ~1% residuals) due primarily to the lower S/N of their spectrum. Their fit agrees quite well with our finding of a ~1 Gyr old population in the nucleus and our best-fit reddening. Unlike us, they find no evidence for young stars, probably because the NGC 205 template spectrum used for intermediate ages also includes a young stellar component (e.g., Monaco et al. 2009). The nuclear stellar populations have also been recently studied by Bouchard et al. (2010) using a different fitting code and stellar library. Their best-fit four-component model matches ours very well, with 4% of the light in stars younger than 150 Myr, 20% at 430 Myr, 62% at 1.7 Gyr, and 14% at 12 Gyr.

5.3. Nuclear Cluster Mass-to-light Ratio

The multi-age population fits to the NGC 404 nuclear spectrum are degenerate, with many possible combinations of ages and extinctions giving similar quality fits. This translates into an uncertainty in the stellar population M/L, with the presence of more young stars decreasing the M/L and the presence of more old stars increasing it. For comparison with the dynamical models (Section 6.1), we would like to quantify the range of possible M/Ls allowed by spectral synthesis fits.

To try to quantify the possible variation in the M/L, we took the best-fit model described in the previous section (model 2, with CB07 and current solar metallicity) and fixed the age of each individual SSP (e.g., just the 10 Gyr population) to have between 0%–100% of the flux of the unconstrained best-fit model, while the extinction and contribution of the rest of the SSPs were allowed to vary. We then took all "acceptable" fits (defined below) and examined the range in M/L. Because we have SB profiles in both I and H bands (Figure 3), we focus on the M/Ls in those bands.

We choose to consider all fits with reduced χ^2 values of < 5 as acceptable, a value 18% higher than our best-fitting models. This choice is informed by the χ^2 probability distribution; our fits have ~660 degrees of freedom and ignoring any model errors, the 99% confidence limit for this distribution is a $\Delta\chi^2$ of 13%. Unfortunately, since our best fit has a reduced χ^2 of 4.2, there must be significant deficiencies in the models or flux calibration at the 1% level. Nonetheless, the range of M/Ls with reduced $\chi^2 < 5$ should reflect a conservative estimate of the acceptable values, roughly equivalent to 3σ error bars.

We find that the range of acceptable M/Ls is 0.68–1.22 in the I band and 0.29–0.61 in the H band. We note that the best-fit M/Ls of 0.73 in the I band and 0.34 in the H band are near to the lower range of these values, suggesting a larger degeneracy in the mass of old stars than for the younger populations. Our best-fit values are consistent with the dynamical $M/L_I = 0.70\pm0.04$ derived in Section 6.1.

5.4. Bulge Stellar Populations

In Cid Fernandes et al. (2005), they analyze the radial variations in the NGC 404 spectrum and find increasing age with radius, with the old and intermediate age templates having equal weight at radii between 5″ and 10″. We use our MMT spectra of NGC 404 to extract the spectra at radii between 5″ and 10″ from the nucleus. From our profile fits (Figure 3), we expect that the bulge component should dominate this spectrum. This spectrum has a peak S/N of 70 around 5000 Å dropping to 25 at 3700 Å.

The models that best fit the NGC 404 bulge spectrum are the same sets of models as the nuclear spectrum (i.e., model 1 with $Z = 0.008$ and model 2). However, like Cid Fernandes et al. (2005) we find that the bulge has a significantly older population with all the best fits having >50% of the light in an old ($\geqslant 5$ Gyr) component. The best fits have A_V between 0.16 and 0.24 which corresponds well to the A_V of 0.19 expected for the foreground extinction (Schlegel et al. 1998) and is consistent with the dust absorption being primarily restricted to the inner 5″ of the galaxy as suggested by *HST* color images. The best fits all have residuals of ~2.6%, corresponding to a reduced χ^2 of 2.0. All the fits have ~2% of the light in a young (<100 Myr) component and a significant contribution (~30%) from a ~1 Gyr component. This analysis clearly shows a significant population difference between the bulge and the nuclear spectrum which supports the separation of the SB profiles into separate components in Section 3.

As all the models have nearly identical fits, we infer M/L ratio using model 2, which best fits the NSC spectrum. We find M/Ls of 1.69, 1.28, and 0.63 in the V, I, and H bands.

Two contemporaneous papers suggest that a dominant old population extends out to larger radii as well. At $r \sim 25''$, Bouchard et al. (2010) find that two-thirds of the mass are an old component using spectral synthesis. And using a deep color–magnitude diagram at a radius of ~160″ (near the disk–bulge transition), Williams et al. (2010) have found ~80% of the stellar mass is >10 Gyr old. The nucleus, with its dominant intermediate age population, is therefore quite distinct from the rest of the galaxy.

6. DYNAMICAL MODELING

In this section, we present dynamical modeling of the central mass distribution of NGC 404 using both the stellar (absorption line) and gas (H_2 emission) kinematics. From modeling of the

stellar kinematics, we find an $M/L_I = 0.70 \pm 0.04$. We can use this to derive a total mass for the NSC by combining this estimate with the total luminosity of the NSC and central excess (Table 2) to get a mass of $(1.1 \pm 0.2) \times 10^7 \, M_\odot$. The error on the NSC mass includes additional uncertainty due to the possible variation in M/L of the central excess. We note that the dynamical M/L_I matches the best-fit M/L_I derived from the stellar population fits to within 10%.

We can also constrain the presence of an MBH using the dynamical models. The two methods give inconsistent results for the BH mass, with the stellar kinematics suggesting an upper limit of $<1 \times 10^5 \, M_\odot$, while the gas models are best fitted with an MBH of mass $4.5^{+3.5}_{-2} \times 10^5 \, M_\odot$ (3σ errors). These measurements assume a constant M/L within the NSC; taking into account possible variations of M/L at very small radii, the BH mass estimates/upper limits can increase by up to $3 \times 10^5 \, M_\odot$. If there is an MBH in NGC 404, its mass is constrained to be $<10^6 \, M_\odot$, smaller than any previous dynamical BH mass measurement in a present-day galaxy.

6.1. Stellar Dynamical Model

We constructed a dynamical model to estimate the mass and M/L of the NSC and of a possible central MBH inside it. The first step in this process is developing a model for the light distribution. To parameterize the SB distribution of NGC 404 and deproject the SB into three dimensions, we adopted a multi-Gaussian expansion (MGE; Emsellem et al. 1994). The MGE fit was performed with the method and software[10] of Cappellari (2002). We fit a two-dimensional (2D) form of the I-band data as presented in Section 3: at $r < 5''$, we use the WFPC2 I-band image with reddened regions masked out, while outside of $5''$, we use the ACS data (which is saturated in the nucleus). Although the use of NIR data would be preferable given the presence of dust in the nucleus, the uncertainty in the NIFS PSF and the poor resolution and sampling of the available *HST* NICMOS data makes the *F814W* data the best available image. The MGE fit takes into account the PSF: we use a Tiny Tim PSF (Krist 1995). In the fit, we forced the observed axial ratios q' of the MGE Gaussians to be as big as possible, not to artificially constrain the allowed inclination of the model. The PSF-convolved MGE represents a reasonable match to the *F814W*-band images with some mismatch seen in the inner parts due to dust. We note that modeling results based on NICMOS *F160W* mass models are consistent with those presented here.

The primary uncertainty in the determination of $M_{\rm BH}$ results from uncertainties in the central stellar mass profile. The *F814W* luminosity at $r < 0''.05$ (0.7 pc) is $\sim 1.3 \times 10^6 \, L_\odot$, while the MGE model has a luminosity of $\sim 4 \times 10^5 \, L_\odot$ within a sphere of the same radius. Translating this luminosity into a stellar mass density is complicated given the possible presence of dust, stellar population gradients, nonthermal emission, and possible nuclear variability. Furthermore, the available kinematics sample only the very nuclear $R \lesssim 1''.5$ region of the galaxy. This spatial coverage is not sufficient to uniquely constrain the orbital distribution and $M_{\rm BH}$ in NGC 404 (Shapiro et al. 2006; Krajnović et al. 2009). This complex situation does not justify the use of general brute-force orbital superposition dynamical modeling methods (e.g., Richstone & Tremaine 1988; van der Marel et al. 1998). This implies we will not be able to uniquely prove the existence of a BH in this galaxy, but we can still explore the ranges of allowed $M_{\rm BH}$ by making some simplifying
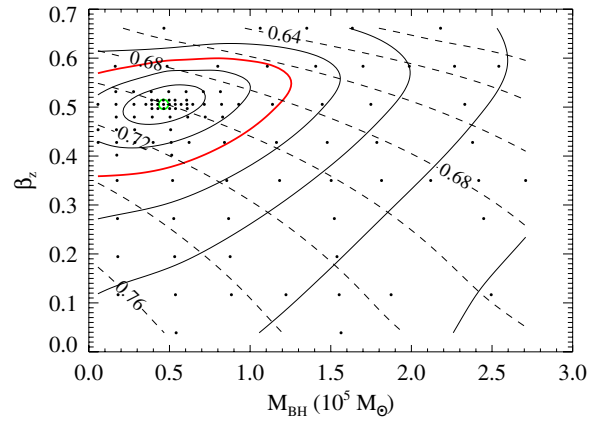
---

[10] Available from http://purl.org/cappellari/idl/

Figure 14. χ^2 contours describing the agreement between the JAM dynamical models and the NIFS integral-field observations of $V_{\rm rms}$. The models optimize the three parameters $M_{\rm BH}$, β_z, and M/L but the contours are marginalized over the M/L, which is overplotted as dashed contours with labels. Dots show the grid of models. The three lowest χ^2 contour levels represent the $\Delta\chi^2 = 1$, 4, and 9 (thick red line) corresponding to 1, 2, and 3σ confidence levels for one parameter.

(A color version of this figure is available in the online journal.)

observationally motivated assumptions. A similar, but less general approach was used in other studies of BHs in NSCs from stellar kinematics (Filippenko & Ho 2003; Barth et al. 2009). We note that because we kinematically resolve the NSC and can determine its M/L, we can provide stricter BH upper limits than those provided by these papers, in which the NSC kinematics were unresolved.

The adopted dynamical model uses the Jeans Anisotropic MGE (JAM) software[10] which implements an axisymmetric solution of the Jeans equations which allow for orbital anisotropy (Cappellari 2008). Once a cylindrical orientation for the velocity ellipsoid has been assumed, parameterized by the anisotropy parameter $\beta_z = 1 - \sigma_z^2/\sigma_R^2$, the model gives a unique prediction for the observed second velocity moments $V_{\rm rms} = \sqrt{V^2 + \sigma^2}$, where V is the mean stellar velocity and σ is the velocity dispersion. The JAM models appear to provide good descriptions of integral-field observations of large samples of real lenticular galaxies (Cappellari 2008; Scott et al. 2009) and give similar estimates for BH masses as Schwarzschild models (Cappellari et al. 2010).

The luminous matter likely dominates in the extreme high-density nucleus of NGC 404. For this dynamical model, we assume light traces mass with a constant M/L. For the model we assumed a nearly face-on inclination of $i = 20°$ ($i = 90°$ being edge-on) as indicated by the regular H I disk kinematics and geometry (del Río et al. 2004), and further supported by the nearly circular isophotes at small radii. However, unlike the gas dynamical model, our results do not depend strongly on this inclination assumption. The model has three free parameters: (1) the anisotropy β_z, (2) the mass of a central supermassive BH, $M_{\rm BH}$, and (3) the I-band total dynamical M/L. To find the best-fitting model parameters we constructed a grid for the two nonlinear parameter (β_z, $M_{\rm BH}$) values and for each pair we linearly scaled the M/L to match the data in a χ^2 sense. The resulting contours of χ^2, marginalized over M/L, are presented in Figure 14. They show that with the assumed stellar mass distribution, the models suggest an $M_{\rm BH} < 1 \times 10^5 \, M_\odot$ with $\beta_z \sim 0.5$ and $M/L = 0.70 \pm 0.04 \, M_\odot/L_\odot$ in the I band (3σ levels or $\Delta\chi^2 = 9$). A corresponding data–model comparison
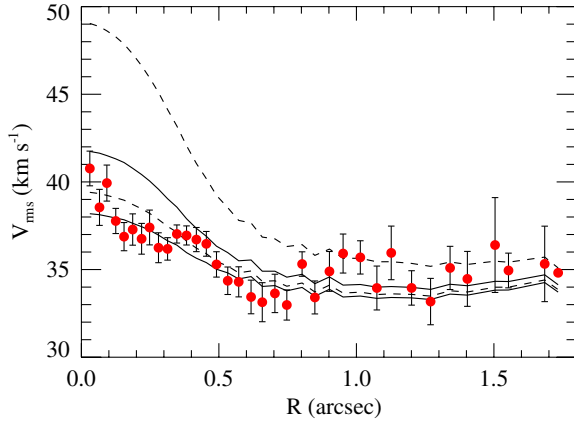
Figure 15. Observed NIFS profiles of V_{rms}, biweight averaged over circular annuli (data points), are compared to JAM model predictions of the same quantity, for different $M_{\mathrm{BH}} = 0$ (lowest solid line), 1, 3, and $10 \times 10^5 \, M_\odot$ (top dashed line). All models have $M/L_I = 0.70 \, M_\odot/L_\odot$ and $\beta_z = 0.5$ as the best-fitting solution.

(A color version of this figure is available in the online journal.)

is shown in Figure 15. The dynamical M/L_I (which includes a correction for foreground extinction) is quite close to our best-fit stellar population estimate of $M/L_I = 0.73$.

As noted above, the largest uncertainty in our MBH measurements comes from uncertainty in the central stellar mass density hidden by the assumption of a constant M/L. The bluer color in the $F547M - F814W$ color image (Figure 2) and the presence of UV emission at $r \lesssim 0\rlap{.}{''}05$ suggest a possible decrease in M/L which could mask the presence of a possible BH. Because our optical spectroscopy does not resolve the central structures, we can only use the *HST* imaging data to try constraining possible variations in the M/L. We now determine a limit on how much the central M/L may vary by quantitatively examining the color difference between the NSC and the central pixels. We measured the NSC colors just to the west of the nucleus and find an $F330W - F547M$ ($U - V$) of 0.48 and an $F547 - F814W$ ($V - I$) of 0.87 after correction for foreground reddening. The colors at $r < 0\rlap{.}{''}05$ are both about 0.1 mag bluer than the NSC colors. In $V-I$ the presence of a $\sim$10 Myr population will give the largest reduction in M/L with the least effect on the color, since these populations are dominated by red supergiants at long wavelengths (e.g., see Figure 4 in Seth et al. 2008b). For a solar metallicity population, the $V - I$ color at 10 Myr is about 0.5 (Girardi et al. 2000), meaning the observed nuclear color difference is consistent with about 30% of the light in young stars. This would result in a $\sim$30% reduction in the M/L, as the M/L for a 10 Myr population is very small. However, this large fraction of a young population would imply a larger change in $U-V$ color than observed, so 30% represents an upper limit on the reduction in M/L. If we take the I-band luminosity at $r < 0\rlap{.}{''}05$ of $1.3 \times 10^6 \, L_\odot$ with our default M/L of 0.70, we get a mass at $r < 0\rlap{.}{''}05$ of $9 \times 10^5 \, M_\odot$. Reducing the M/L by 30% at the center relative to the NSC would therefore reduce the central stellar mass *and increase the BH mass* by $\sim 3 \times 10^5 \, M_\odot$. Therefore, even including the effects of a possible decline in the central M/L, the BH mass is constrained to be $\lesssim 4 \times 10^5 \, M_\odot$ by the stellar dynamical model. Future *HST* spectroscopy that can resolve the stellar population gradient in the nucleus should produce a more accurate mass model that will enable us to robustly test the presence of an MBH in NGC 404.

6.2. Gas Dynamical Model

In addition to the stellar dynamical model, we constructed a dynamical model to reproduce the kinematics of molecular hydrogen emission (Section 4.2) to obtain an additional constraint in the presence of a possible central BH. We follow the modeling approach of Neumayer et al. (2007) that assumes the gas to be settled in a thin disk in the joint potential of the stars and a putative BH. We assume the gas is moving on circular orbits and we do not include a pressure term in the gas model, as the velocity dispersion of the gas is small. We have tested the effect of an additional pressure term and find it to be very small, well below our derived errors. The stellar potential is fixed using the MGE parameters and the stellar M/L_I derived in Section 5.2, and thus suffers from the same uncertainty in the central stellar mass profile.

The gas velocity map appears quite complex with sudden changes in the P.A. of the major kinematic axis, and some of the kinematic features might be due to non-gravitational motions driven by the LINER nucleus. However, as described in Section 4.2, there also appears to be clear rotation in the central $0\rlap{.}{''}4 \times 0\rlap{.}{''}4$ with a major rotation axis of $\sim$15° and a twist to slightly negative P.A.s at larger radii. We interpret this twist in the line of nodes as a change in the inclination angle of the molecular gas disk and model the kinematics using a tilted ring model. The inclination angle of the gas disk for radii $> 0\rlap{.}{''}2$ is fixed to the value of 20° that is also used for the stellar model and consistent with inclinations derived by del Río et al. (2004) from H I. The dynamical model has two free parameters: (1) the inclination angle of the inner ($r \leqslant 0\rlap{.}{''}2$) H_2 disk i and (2) the mass of a central supermassive BH M_{BH}. To find the best-fitting model parameters, we constructed a grid for the two parameters (i, M_{BH}) and matched the data (velocity and velocity dispersion) minimizing χ^2. Figure 17 shows the contours of χ^2 and indicates the best-fit model parameters $i = 37° \pm 10°$ and $M_{\mathrm{BH}} = 4.5^{+3.5}_{-2.0} \times 10^5 \, M_\odot$ (3σ errors). The best-fitting model for the H_2 velocity field is compared to the data in Figure 16. We note that the best-fit inclination is consistent with the axial ratios of the emission (Section 4.2).

As Figure 17 shows, the inclination angle i and the central mass M_{BH} are strongly coupled, since the amplitude of the rotation curve is proportional to $\sqrt{M_{\mathrm{BH}}} \times \sin(i)$. This degeneracy in the gas model leads to the relatively large uncertainties in inclination angle and BH mass. However, the gas kinematics cannot be reproduced without a central BH, even for an almost edge-on central inclination angle. The best-fitting BH mass is significantly different from the non-detection of $<1 \times 10^5 \, M_\odot$ derived from the stellar kinematics. One possible source of this discrepancy would be non-gravitational motions that are not accounted for by the gas-kinematical model. Another possible problem is the assumption of a thin gas disk, although thicker gas distributions provided worse fits to the gas-kinematic data. We note that both determinations use the same MGE mass model, and thus the uncertainty due to the central M/L applies to these results as well. This could increase the BH mass estimates by as much as $3 \times 10^5 \, M_\odot$.

7. DISCUSSION

7.1. Nuclear Star Cluster: Scaling Relationships and Formation

We compare the NGC 404 NSC to the scaling relationships between galaxy/bulge mass and BH/NSC mass in Figure 18. We have derived the mass of the NSC using the dynamical M/L
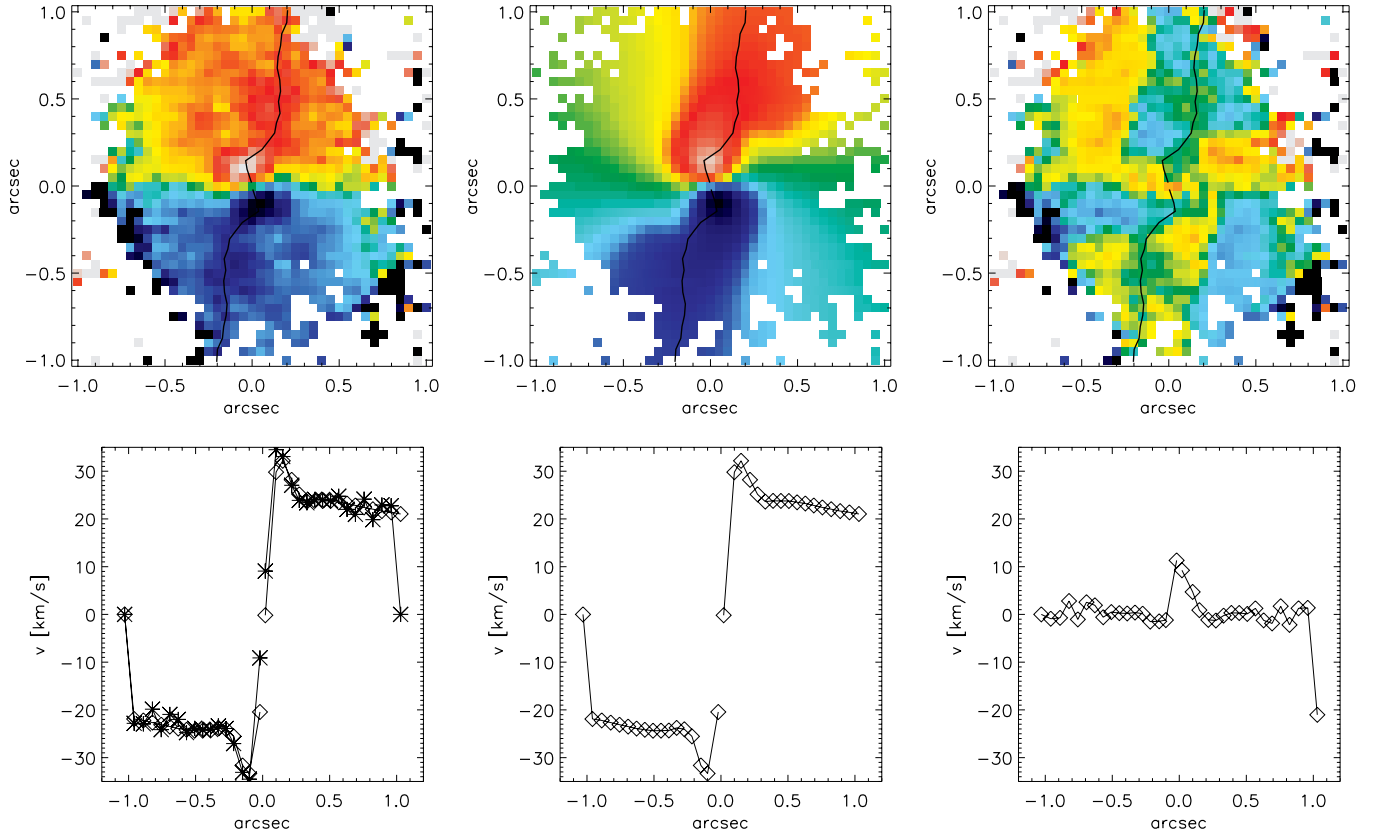
Figure 16. Velocity field of the best-fitting H$_2$ dynamical model (middle, top), with a BH mass of $M_{BH} = 4.5 \times 10^5$ $M_\odot$ and a disk inclination of 37°, in comparison to the symmetrized data (top left). The velocity residual (data model) is shown in the right panel. The velocity curves in the bottom panels are extracted along the line of nodes (overplotted to the velocity maps) and represent the peak velocity curves. The diamonds correspond to the model velocity curve, while the crosses correspond to the data.

(A color version of this figure is available in the online journal.)

Figure 17. Constraining the mass of the central BH: the figure indicates the grid of models (in BH mass, M_{BH}, and disk inclination) that was calculated, and the contours show χ^2 in the vicinity of the best-fit dynamical models for matching the H$_2$ kinematics. The minimum χ^2 model is at $M_{BH} \sim 4.5 \times 10^5$ $M_\odot$ and a disk inclination of 37°. The contours indicate the 1, 2, and 3σ confidence levels, respectively (see the text for details).

Figure 18. Scaling relations for NSCs and MBHs in early-type galaxies. Data for MBHs are from Häring & Rix (2004), while for the NSCs these are from Côté et al. (2006) with mass estimates from Seth et al. (2008a). The solid line shows the joint MBH/NSC fit from Ferrarese et al. (2006), while the dashed line shows the fit to the MBH data from Häring & Rix (2004). Just the bulge mass is plotted for NGC 404; the total galaxy mass would be ~30% larger.

(A color version of this figure is available in the online journal.)

determined from the NIFS stellar kinematics and the luminosity of the NSC (and central excess) above the underlying bulge. The NGC 404 NSC mass is a large fraction (1%–2%) of the bulge/galaxy mass, making it fall significantly above the relationship for MBHs and early-type Virgo NSCs given by Ferrarese et al. (2006); however, there are several other similar outliers in the
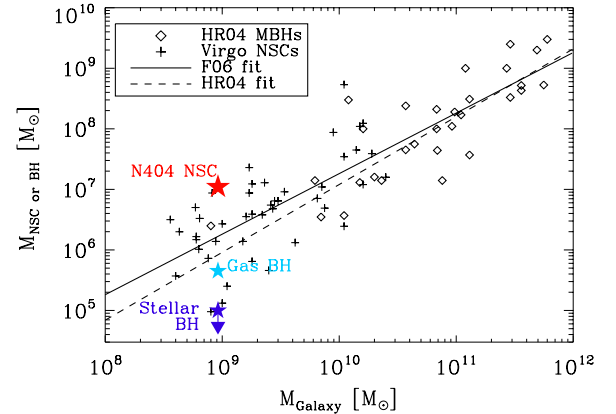
Virgo NSC sample. Using the Ferrarese et al. (2006) NSC mass versus σ relation also gives a mass nearly an order of magnitude smaller than the measured NSC mass.

The NSCs high mass relative to its galaxy raise the question of whether our interpretation of this component as an NSC is correct. As an alternative, we could be seeing some form of
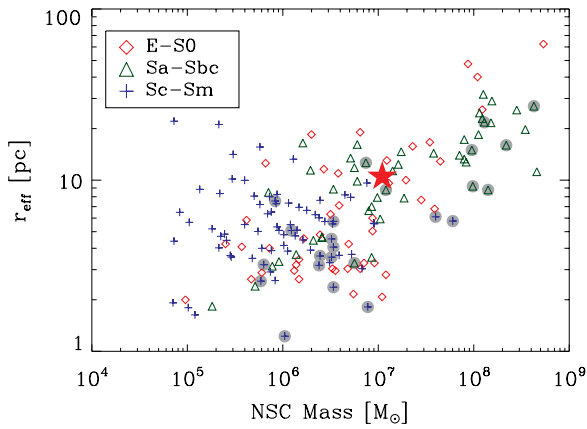
Figure 19. Mass vs. size for NSCs collected in Seth et al. (2008a). The large solid star shows the position of the NGC 404 NSC, showing that it has a size and mass typical of other early-type galaxies. Data are from Carollo et al. (1997, 1998, 2002), Böker et al. (2002), Côté et al. (2006), and Seth et al. (2006). Points with underlying gray dots have dynamical or spectroscopic M/L estimates from Walcher et al. (2005) and Rossa et al. (2006).

(A color version of this figure is available in the online journal.)

"extra-light component" (Rothberg & Joseph 2004; Hopkins et al. 2009; Kormendy et al. 2009) or an "extended nuclear source" (Balcells et al. 2007) that are typically seen on somewhat larger scales than NSCs in coreless elliptical, lenticular, and early-type spirals. The mass fraction of ∼1% places the NGC 404 NSC in the regime of overlap between NSCs and the extra-light components (Figure 46 of Hopkins et al. 2009).

Using data collected in Seth et al. (2008a), we plot the size and mass of clusters in Figure 19 and find that the NSC in NGC 404 is typical of those in other early-type galaxies. The NGC 404 NSC is also typical in the mass–density plane, and the NSC Sérsic index of ∼2 is similar to that found for the M32 and Milky Way NSC in (Graham & Spitler 2009). The morphology of the NGC 404 NSC is therefore completely consistent with other NSCs. Its mass and density are also similar to the lowest mass extra-light components (Hopkins et al. 2009, Figure 45) and follow the size-SB scaling of the extended nuclear components (Figure 3 of Balcells et al. 2007). In Hopkins et al. (2009), they argue that while the extra light and NSCs can overlap in morphological properties, the two can still be distinguished based on their kinematics and stellar populations. We disagree with their argument. Kinematically, both NSCs and extra light can be disky and rotating (Krajnović et al. 2008; Seth et al. 2008b; Trippe et al. 2008) and in early-type galaxies, the stellar populations of many NSCs are not significantly different from their underlying galaxy (Côté et al. 2006; Rossa et al. 2006). We therefore suggest that the distinction between extra-light components and NSCs may be ambiguous in some cases such as NGC 404.

The extra-light components in elliptical galaxies are thought to result from gas funneled to the center of the galaxy during gas-rich mergers (e.g., Mihos & Hernquist 1994; Hopkins et al. 2009). Given the complicated kinematics and stellar population of the NGC 404 NSC, it must be formed from multiple episodes of nuclear accretion. However, it formed about half its stars 1–3 Gyr ago. In del Río et al. (2004), they suggest NGC 404 underwent a merger with a gas-rich dwarf ∼1 Gyr ago to explain the presence of the H I gas disk observed at large radii. The age estimate of the merger was based on the radius beyond which the gas had not yet settled onto the galaxy plane. It is therefore plausible that the ∼ 6×10^6 $M_\odot$ of stars formed at about this

same age in the NSC resulted from accumulation of merger gas at the center of the galaxy. A merger origin is also consistent with the presence of counter-rotation in the central excess. This scenario is quite different from the formation mechanism suggested by observations of late-type galaxies (Seth et al. 2006, 2008b; Walcher et al. 2006), which appear to form primarily by episodic accretion of material (gas or stars) from the galaxy disk. Resolved observations of a larger sample of NSCs in early-type galaxies are required to determine if NGC 404 is an unusual case, or if NSCs in early-type galaxies typically show some evidence gas accreted from mergers.

7.2. The Possible NGC 404 MBH

Our dynamical modeling in Section 6 provides mixed evidence for the presence of an MBH in NGC 404 with mass less than 10^6 $M_\odot$ (making it an IMBH candidate). If verified through follow-up observations, this BH would be the lowest mass dynamically detected BH at the center of a galaxy, with previous determinations of low-mass BHs in M32 (($2.5 \pm 0.5) \times 10^6$ $M_\odot$; Verolme et al. 2002) and Circinus (($1.7 \pm 0.3) \times 10^6$ $M_\odot$; Greenhill et al. 2003) being significantly more massive. A reverberation mapping mass of the BH in nearby Seyfert 1 galaxy NGC 4395 (Peterson et al. 2005) and indirect mass measurements in other low-mass Seyfert 1 galaxies (e.g., Greene & Ho 2007) provide additional evidence for the presence of IMBHs at the centers of lower mass galaxies. Possible IMBHs at the center of star clusters (and possible former nuclei) G1 (Gebhardt et al. 2005), ω Cen (Noyola et al. 2008; van der Marel & Anderson 2010), and M54 (Ibata et al. 2009) suggest that IMBHs with masses of 10^4–10^5 $M_\odot$ may be widespread, but these results remain controversial. Measuring the occupation fraction and mass of BHs in galaxies like NGC 404 is key to understanding the formation of MBHs in general (Volonteri et al. 2008).

From the latest version of the M_{BH}–σ relations for different galaxy samples from Gültekin et al. (2009), the predicted M_{BH} ranges from 0.8 to 3×10^5 $M_\odot$ for a bulge σ of 35–40 km s^{-1}. This range of masses is consistent with all our dynamical BH mass estimates. A somewhat higher mass (8×10^5 $M_\odot$) is implied by the Häring & Rix (2004) relationship (see Figure 18) and is consistent only with the gas-dynamical estimate, while the Ferrarese et al. (2006) relationships have masses $> 10^6$ $M_\odot$ and are thus inconsistent with our data. If a BH with a few $\times 10^5$ $M_\odot$ resides in the center of NGC 404, better knowledge of the mass model from future *HST* observations should enable us to detect it.

The relative mass of NSCs and BHs within a single galaxy can probe the relationship of these two objects. Seth et al. (2008a) find that the relative mass of BHs and NSCs is of order unity (with a scatter of at least 1 order of magnitude), while Graham & Spitler (2009) suggest a possible evolution in the relative mass with the least massive galaxies being NSC dominated and the most massive galaxies being BH dominated. The BH in NGC 404 is <10% of the NSC mass and thus is not an obvious outlier from other galaxies where the mass of both objects is known.

Finally, we note that the evidence of variability in the UV spectrum (Maoz et al. 2005) and possibly the NIR dust emission (Section 3.1), suggests that the NGC 404 BH accretion is variable. In both cases, the observed flux decreased from observations taken in the 1990s to those taken in the last decade. This might help explain the ambiguous nature of the AGN indicators in the NGC 404 nucleus; emission that originates near the BH (e.g., hard X-ray emission, broad Hα) may have recently

disappeared, while the narrow-line region located at tens of parsecs, may continue to show signs of the earlier accretion. However, the observed hot-dust emission suggests that the BH may still be accreting at a very low level.

8. CONCLUSIONS AND FUTURE PROSPECTS

This paper is the second resulting from our survey of nearby NSCs, and demonstrates the rich detail we can obtain for these objects. The NGC 404 nucleus is a complicated environment, with both an NSC and a possible BH. We have found that the SB profile of the inner part of NGC 404 suggests the galaxy can be broken into three components: (1) a bulge that dominates the light beyond $1''$, with $M_{bulge} \sim 9 \times 10^8\ M_\odot$, $r_{eff} = 640$ pc, and a Sérsic index of ~ 2.5; (2) an NSC that dominates the light in the central arcsecond with $r_{eff} = 10$ pc and a dynamical mass of $(1.1 \pm 0.2) \times 10^7\ M_\odot$; and (3) a central excess at $r < 0''.2$, composed of younger stars, dust emission, and perhaps AGN continuum. NIFS IFU spectroscopy shows that the NSC has modest rotation along roughly the same axis as the H I gas at larger radii, while the central excess counter-rotates relative to the NSC. Furthermore, molecular gas traced by H_2 emission shows rotation perpendicular to the stellar rotation. A stellar population analysis of optical spectra indicates that half of the stars in the NSC formed ~ 1 Gyr ago. Some ancient and very young (< 10 Myr) stars are also present. This SFH is dramatically different from the rest of NGC 404, which is dominated by stellar populations > 5 Gyr in age. We suggest a possible scenario where the burst of star formation in the NSC ~ 1 Gyr ago resulted from the accretion of gas into the galaxy center during a merger. This formation scenario is quite different from the episodic disk accretion suggested by observations NSCs in late-type galaxies.

Our dynamical modeling of the stellar and gas kinematics provide mixed evidence for the presence of a BH in NGC 404. Assuming a constant M/L within the nucleus, the stellar dynamical model suggests an upper limit of $1 \times 10^5\ M_\odot$, as well as measuring an $M/L_I = (0.70 \pm 0.04)$ for the NSC. The gas kinematics are best fitted by models including the presence of a BH with $M_{BH} = 4.5^{+3.5}_{-2.0} \times 10^5\ M_\odot$. Both dynamical BH mass estimates rely on a model for the stellar mass that we construct from *HST* $F814W$-band imaging. Uncertainties in the light profile (due to variability) and M/L (due to stellar population changes) within the central excess are of the same order as the difference between the two BH mass estimates. We have proposed to measure the mass model by using *HST*/STIS spectroscopy to resolve the stellar populations within the nucleus and additional multi-band imaging to extend this model to two dimensions. If successful we will combine this mass model with the kinematic observations presented here as well as larger-scale kinematics obtained from the MMT to more robustly determine the BH mass.

In addition to the direct evidence of the BH from the dynamical models, we find two other properties of the nucleus which suggest the presence of an AGN. First, we find unresolved hot-dust emission at the center of the NSC with a luminosity of $\sim 1.4 \times 10^{38}$ erg s^{-1}. Comparison of the NIFS light profile to previous NICMOS observations suggests that this dust emission may be variable as is seen in other AGNs. Second, the H_2 line ratios within the central arcsecond indicate thermal excitation in dense gas similar to what is seen in other AGNs. Our proposed *HST* observations request multi-epoch UV through NIR imaging to search for definitive evidence of BH accretion in NGC 404.

Our nearby NSC survey includes 13 galaxies within 5 Mpc with M_B between -15.9 and -18.8 for which we will have comparable data to that presented here obtained using MMT, Very Large Telescope (VLT), and Gemini. These galaxies span a wide range of Hubble types in which we can examine the process of NSC formation; there are four early-type E/S0 galaxies and nine spirals of type Sc and later. NGC 404 represents one of the stronger cases for finding a BH, given its LINER emission and proximity. However, we expect to be able to detect or place upper limits of $\lesssim 10^5\ M_\odot$ on BHs in each of the sample galaxies.

REFERENCES

Abel, N. P., & Satyapal, S. 2008, ApJ, 678, 686
Alonso-Herrero, A., Ward, M. J., & Kotilainen, J. K. 1996, MNRAS, 278, 902
Baggett, W. E., Baggett, S. M., & Anderson, K. S. J. 1998, AJ, 116, 1626
Balcells, M., Graham, A. W., & Peletier, R. F. 2007, ApJ, 665, 1084
Barth, A. J., Ho, L. C., & Sargent, W. L. W. 2002, AJ, 124, 2607
Barth, A. J., Strigari, L. E., Bentz, M. C., Greene, J. E., & Ho, L. C. 2009, ApJ, 690, 1031
Bartko, H., et al. 2009, ApJ, 697, 1741
Bertelli, G., Bressan, A., Chiosi, C., Fagotto, F., & Nasi, E. 1994, A&AS, 106, 275
Bessell, M. S. 1999, PASP, 111, 1426
Böker, T., Laine, S., van der Marel, R. P., Sarzi, M., Rix, H.-W., Ho, L. C., & Shields, J. C. 2002, AJ, 123, 1389
Bouchard, A., Prugniel, P., Koleva, M., & Sharina, M. 2010, A&A, in press (arXiv:1001.4087)
Bruzual, G., & Charlot, S. 2003, MNRAS, 344, 1000
Cappellari, M. 2002, MNRAS, 333, 400
Cappellari, M. 2008, MNRAS, 390, 71
Cappellari, M., & Copin, Y. 2003, MNRAS, 342, 345
Cappellari, M., & Emsellem, E. 2004, PASP, 116, 138
Cappellari, M., et al. 2010, in AIP Conf. Ser., in press (arXiv:1001.3233)
Cardelli, J. A., Clayton, G. C., & Mathis, J. S. 1989, ApJ, 345, 245
Carollo, C. M., Stiavelli, M., de Zeeuw, P. T., & Mack, J. 1997, AJ, 114, 2366
Carollo, C. M., Stiavelli, M., & Mack, J. 1998, AJ, 116, 68
Carollo, C. M., Stiavelli, M., Seigar, M., de Zeeuw, P. T., & Dejonghe, H. 2002, AJ, 123, 159
Charlot, S., & Fall, S. M. 2000, ApJ, 539, 718
Cid Fernandes, R., González Delgado, R. M., Storchi-Bergmann, T., Martins, L. P., & Schmitt, H. 2005, MNRAS, 356, 270
Cid Fernandes, R., et al. 2004, ApJ, 605, 105
Côté, P., et al. 2006, ApJS, 165, 57
del Río, M. S., Brinks, E., & Cepa, J. 2004, AJ, 128, 89
Dudik, R. P., Satyapal, S., Gliozzi, M., & Sambruna, R. M. 2005, ApJ, 620, 113
Emsellem, E., Monnet, G., & Bacon, R. 1994, A&A, 285, 723
Eracleous, M., Shields, J. C., Chartas, G., & Moran, E. C. 2002, ApJ, 565, 108
Ferrarese, L., et al. 2000, ApJ, 529, 745
Ferrarese, L., et al. 2006, ApJ, 644, L21
Filippenko, A. V., & Ho, L. C. 2003, ApJ, 588, L13
Filippenko, A. V., & Sargent, W. L. W. 1989, ApJ, 342, L11
Gebhardt, K., Rich, R. M., & Ho, L. C. 2005, ApJ, 634, 1093
Gebhardt, K., et al. 2000, ApJ, 539, L13
Gebhardt, K., et al. 2001, AJ, 122, 2469

Genzel, R., Thatte, N., Krabbe, A., Kroker, H., & Tacconi-Garman, L. E. 1996, ApJ, 472, 153

Ghez, A. M., et al. 2008, ApJ, 689, 1044

Girardi, L., Bressan, A., Bertelli, G., & Chiosi, C. 2000, A&AS, 141, 371

Gogarten, S. M., et al. 2009, ApJ, 691, 115

González-Martín, O., Masegosa, J., Márquez, I., Guerrero, M. A., & Dultzin-Hacyan, D. 2006, A&A, 460, 45

Graham, A. W. 2008, PASA, 25, 167

Graham, A. W., & Driver, S. P. 2005, PASA, 22, 118

Graham, A. W., & Guzmán, R. 2003, AJ, 125, 2936

Graham, A. W., & Spitler, L. R. 2009, MNRAS, 397, 2148

Greene, J. E., & Ho, L. C. 2004, ApJ, 610, 722

Greene, J. E., & Ho, L. C. 2007, ApJ, 670, 92

Greenhill, L. J., et al. 2003, ApJ, 590, 162

Gültekin, K., et al. 2009, ApJ, 698, 198

Häring, N., & Rix, H.-W. 2004, ApJ, 604, L89

Hicks, E. K. S., Davies, R. I., Malkan, M. A., Genzel, R., Tacconi, L. J., Sánchez, F. M., & Sternberg, A. 2009, ApJ, 696, 448

Ho, L. C. (ed.) 2004, in Carnegie Observatories Centennial Symposia, Coevolution of Black Holes and Galaxies (Cambridge: Cambridge Univ. Press), 292

Ho, L. C., Filippenko, A. V., & Sargent, W. L. W. 1997, ApJS, 112, 315

Hopkins, P. F., Cox, T. J., Dutta, S. N., Hernquist, L., Kormendy, J., & Lauer, T. R. 2009, ApJS, 181, 135

Hopkins, P. F., & Quataert, E. 2010, MNRAS, submitted (arXiv:1002.1079)

Ibata, R., et al. 2009, ApJ, 699, L169

Jarrett, T. H., Chester, T., Cutri, R., Schneider, S. E., & Huchra, J. P. 2003, AJ, 125, 525

Karachentsev, I. D., Karachentseva, V. E., Huchtmeier, W. K., & Makarov, D. I. 2004, AJ, 127, 2031

Kennicutt, R. C., Jr. 1998, ApJ, 498, 541

Kewley, L. J., & Dopita, M. A. 2002, ApJS, 142, 35

Koleva, M., Prugniel, P., Ocvirk, P., Le Borgne, D., & Soubiran, C. 2008, MNRAS, 385, 1998

Kormendy, J., Fisher, D. B., Cornell, M. E., & Bender, R. 2009, ApJS, 182, 216

Kormendy, J., & Richstone, D. 1995, ARA&A, 33, 581

Krajnović, D., Cappellari, M., de Zeeuw, P. T., & Copin, Y. 2006, MNRAS, 366, 787

Krajnović, D., McDermid, R. M., Cappellari, M., & Davies, R. L. 2009, MNRAS, 399, 1839

Krajnović, D., et al. 2008, MNRAS, 390, 93

Krist, J. 1995, in ASP Conf. Ser. 77, Astronomical Data Analysis Software and Systems IV, ed. R. A. Shaw, H. E. Payne, & J. J. E. Hayes (San Francisco, CA: ASP), 349

Kroupa, P., Tout, C. A., & Gilmore, G. 1993, MNRAS, 262, 545

Le Borgne, J.-F., et al. 2003, A&A, 402, 433

Lira, P., Lawrence, A., & Johnson, R. A. 2000, MNRAS, 319, 17

Long, K. S., Charles, P. A., & Dubus, G. 2002, ApJ, 569, 204

Lu, J. R., Ghez, A. M., Hornstein, S. D., Morris, M. R., Becklin, E. E., & Matthews, K. 2009, ApJ, 690, 1463

Magorrian, J., et al. 1998, AJ, 115, 2285

Maoz, D., Koratkar, A., Shields, J. C., Ho, L. C., Filippenko, A. V., & Sternberg, A. 1998, AJ, 116, 55

Maoz, D., Nagar, N. M., Falcke, H., & Wilson, A. S. 2005, ApJ, 625, 699

Maraston, C. 2005, MNRAS, 362, 799

Marigo, P., & Girardi, L. 2007, A&A, 469, 239

Marigo, P., Girardi, L., Bressan, A., Groenewegen, M. A. T., Silva, L., & Granato, G. L. 2008, A&A, 482, 883

Mihos, J. C., & Hernquist, L. 1994, ApJ, 437, L47

Monaco, L., Bellazzini, M., Ferraro, F. R., & Pancino, E. 2005, MNRAS, 356, 1396

Monaco, L., Saviane, I., Perina, S., Bellazzini, M., Buzzoni, A., Federici, L., Fusi Pecci, F., & Galleti, S. 2009, A&A, 502, L9

Mouri, H. 1994, ApJ, 427, 777

Nagar, N. M., Falcke, H., & Wilson, A. S. 2005, A&A, 435, 521

Neumayer, N., Cappellari, M., Reunanen, J., Rix, H.-W., van der Werf, P. P., de Zeeuw, P. T., & Davies, R. I. 2007, ApJ, 671, 1329

Noyola, E., Gebhardt, K., & Bergmann, M. 2008, ApJ, 676, 1008

Osterbrock, D. E. 1989, Astrophysics of Gaseous Nebulae and Active Galactic Nuclei (Mill Valley, CA: Univ. Science Books)

Peterson, B. M., et al. 2005, ApJ, 632, 799

Plana, H., Boulesteix, J., Amram, P., Carignan, C., & Mendes de Oliveira, C. 1998, A&AS, 128, 75

Pogge, R. W., Maoz, D., Ho, L. C., & Eracleous, M. 2000, ApJ, 532, 323

Quillen, A. C., McDonald, C., Alonso-Herrero, A., Lee, A., Shaked, S., Rieke, M. J., & Rieke, G. H. 2001, ApJ, 547, 129

Quillen, A. C., Shaked, S., Alonso-Herrero, A., McDonald, C., Lee, A., Rieke, M. J., & Rieke, G. H. 2000, ApJ, 532, L17

Ravindranath, S., Ho, L. C., Peng, C. Y., Filippenko, A. V., & Sargent, W. L. W. 2001, AJ, 122, 653

Reunanen, J., Kotilainen, J. K., & Prieto, M. A. 2002, MNRAS, 331, 154

Richstone, D. O., & Tremaine, S. 1988, ApJ, 327, 82

Richstone, D. O., et al. 1998, Nature, 395, A14

Riffel, R. A., Storchi-Bergmann, T., & McGregor, P. J. 2009, ApJ, 698, 1767

Riffel, R. A., Storchi-Bergmann, T., Winge, C., McGregor, P. J., Beck, T., & Schmitt, H. 2008, MNRAS, 385, 1129

Rodríguez-Ardila, A., Pastoriza, M. G., Viegas, S., Sigut, T. A. A., & Pradhan, A. K. 2004, A&A, 425, 457

Rossa, J., van der Marel, R. P., Böker, T., Gerssen, J., Ho, L. C., Rix, H.-W., Shields, J. C., & Walcher, C.-J. 2006, AJ, 132, 1074

Rothberg, B., & Joseph, R. D. 2004, AJ, 128, 2098

Satyapal, S., Sambruna, R. M., & Dudik, R. P. 2004, A&A, 414, 825

Satyapal, S., Vega, D., Heckman, T., O'Halloran, B., & Dudik, R. 2007, ApJ, 663, L9

Schlegel, D. J., Finkbeiner, D. P., & Davis, M. 1998, ApJ, 500, 525

Schödel, R., et al. 2007, A&A, 469, 125

Scott, N., et al. 2009, MNRAS, 398, 1835

Seth, A. C., Agüeros, M., Lee, D., & Basu-Zych, A. 2008a, ApJ, 678, 116

Seth, A. C., Blum, R. D., Bastian, N., Caldwell, N., Debattista, V. P., & Puzia, T. H. 2008b, ApJ, 687, 997

Seth, A. C., Dalcanton, J. J., Hodge, P. W., & Debattista, V. P. 2006, AJ, 132, 2539

Shapiro, K. L., Cappellari, M., de Zeeuw, T., McDermid, R. M., Gebhardt, K., van den Bosch, R. C. E., & Statler, T. S. 2006, MNRAS, 370, 559

Shields, J. C., Walcher, C. J., Böker, T., Ho, L. C., Rix, H.-W., & van der Marel, R. P. 2008, ApJ, 682, 104

Siegel, M. H., et al. 2007, ApJ, 667, L57

Storchi-Bergmann, T., McGregor, P. J., Riffel, R. A., Simões Lopes, R., Beck, T., & Dopita, M. 2009, MNRAS, 394, 1148

Terashima, Y., Iyomoto, N., Ho, L. C., & Ptak, A. F. 2002, ApJS, 139, 1

Tikhonov, N. A., Galazutdinova, O. A., & Aparicio, A. 2003, A&A, 401, 863

Tremonti, C. A., et al. 2004, ApJ, 613, 898

Trippe, S., et al. 2008, A&A, 492, 419

Valluri, M., Ferrarese, L., Merritt, D., & Joseph, C. L. 2005, ApJ, 628, 137

van der Marel, R. P., & Anderson, J. 2010, ApJ, 710, 1063

van der Marel, R. P., Cretton, N., de Zeeuw, P. T., & Rix, H. 1998, ApJ, 493, 613

Verolme, E. K., et al. 2002, MNRAS, 335, 517

Volonteri, M., Lodato, G., & Natarajan, P. 2008, MNRAS, 383, 1079

Walcher, C. J., Böker, T., Charlot, S., Ho, L. C., Rix, H.-W., Rossa, J., Shields, J. C., & van der Marel, R. P. 2006, ApJ, 649, 692

Walcher, C. J., et al. 2005, ApJ, 618, 237

Wallace, L., & Hinkle, K. 1996, ApJS, 107, 312

Wehner, E. H., & Harris, W. E. 2006, ApJ, 644, L17

Wiklind, T., & Henkel, C. 1990, A&A, 227, 394

Williams, B. F., et al. 2010, ApJ, submitted

Winge, C., Riffel, R. A., & Storchi-Bergmann, T. 2009, ApJS, 185, 186

Winge, C., Storchi-Bergmann, T., Ward, M. J., & Wilson, A. S. 2000, MNRAS, 316, 1

Zhang, W. M., Soria, R., Zhang, S. N., Swartz, D. A., & Liu, J. F. 2009, ApJ, 699, 281